Dynamics of the Atlantic meridional overturning circulation. Part 2: Forcing by winds and buoyancy ☆

F. Schloesser *, R. Furue, J.P. McCreary, A. Timmermann

International Pacific Research Center, University of Hawaii, Honolulu, HI, United States

ABSTRACT

Recently, Schloesser et al. (2012) explored the dynamics of the descending branch of meridional overturning circulations (MOCs), by obtaining analytic solutions to a variable-density, 2-layer model (VLOM) forced only by a surface buoyancy flux. Key processes involved are the poleward thickening of the upper layer along the eastern boundary due to Kelvin-wave adjustments, the westward propagation of that coastal structure by Rossby waves, and their damping by mixing; the resulting zonal pressure gradient causes the surface MOC branch to converge into the northern basin near the eastern boundary.

In this paper, we extend the Schloesser et al. (2012) study to include forcing by a zonal wind stress $\tau^x(y)$. Much of the paper is devoted to the derivation and analysis of analytic solutions to VLOM; for validation, we also report corresponding numerical solutions to an ocean general circulation model (OGCM). Solutions are obtained in a flat-bottom, rectangular basin confined to the northern hemisphere. The buoyancy forcing relaxes upper-ocean density to a prescribed profile $\rho^*(y)$ that increases polewards until it becomes as large as the deep-ocean density at latitude y_2; north of y_2, then, the ocean is homogeneous (a 1-layer system). The wind stress τ^x drives Subtropical and Subpolar Gyres, and in our standard solution the latter extends north of y_2. Vertical diffusion is not included in VLOM (minimized in the OGCM); consequently, the MOC is not closed by upwelling associated with interior diffusion, but rather by flow through the southern boundary of the basin (into a southern-boundary sponge layer in the OGCM), and solutions are uniquely determined by specifying the strength of that flow or the thermocline depth along the tropical eastern boundary.

Solutions forced by τ^x and ρ^* differ markedly from those forced only by ρ^* because water flows across y_2 throughout the interior of the Subpolar Gyre, not just near the eastern boundary. In some of our solutions, the strength of the MOC's descending branch is determined entirely by this wind-driven mechanism, whereas in others it is also affected by Rossby-wave damping near the eastern boundary. Upwelling can occur in the interior of the Subpolar Gyre and in the western-boundary layer, providing "shortcuts" for the overturning circulation; consequently, there are different rates for the convergence of upper-layer water near y_2, $\mathcal{M}_n$, and the export of deep water south of the Subpolar Gyre, $\mathcal{M}$, the latter being a better measure of large-scale MOC strength. When western-boundary upwelling occurs in our solutions, $\mathcal{M}$ is independent of the diapycnal processes in the subpolar ocean.

1. Introduction

Meridional overturning circulations (MOCs) are an important part of the global ocean circulation. Water masses, formed at high latitudes in regions with large heat loss from the ocean to the atmosphere, spread equatorward within deep MOC branches. Conversely, the shallow branches provide the main pathways by which the ocean transports heat poleward (*e.g.*, Ganachaud and Wunsch, 2000). The Atlantic meridional overturning circulation (AMOC)

is particularly important, a major component of the climate system.

1.1. Background

Because of their importance, many studies have explored the processes controlling MOC strength and structure. Analyzing and comparing a hierarchy of model solutions of different dynamical complexity has emerged as a useful strategy for identifying key processes. Near the base of the hierarchy are solutions obtained in flat-bottomed, rectangular ocean basins, and forced by idealized, surface, buoyancy and momentum fluxes.

1.1.1. Density forcing

In many empirical studies analyzing such solutions to ocean general circulation models (OGCMs), the poleward transport that

---

* Corresponding author. Tel.: +1 401 874 6846.
E-mail addresses: schloess@hawaii.edu, schloess@mail.uri.edu (F. Schloesser).

determines the MOC strength, $\mathcal{M}$, is found to be proportional to the near-surface, depth-averaged *meridional* pressure gradient, that is,

$$\mathcal{M} = C \frac{g \Delta \rho}{2 f \rho_o} H_s^2, \tag{1}$$

where g is the acceleration due to gravity, f the value of the Coriolis parameter at some characteristic latitude, $\Delta \rho$ the pole-to-equator difference in surface density, ρ_o a reference density, H_s is a measure of thermocline thickness, and C a non-dimensional proportionality constant (*e.g.*, Bryan, 1987; Marotzke, 1997; De Boer et al., 2010). Relation (1) can also be derived from scaling arguments, assuming that the large-scale transports are in geostrophic balance (Bryan and Cox, 1967; Park and Bryan, 2000). A useful aspect of (1) is that it does not explicitly depend on upwelling mechanisms related to mixing (*e.g.*, Sandström, 1916; Robinson and Stommel, 1959; Munk and Wunsch, 1998; Vallis, 2006) or the wind-forced divergence of the surface flow (Wyrtki, 1961; Toggweiler and Samuels, 1995; Tsujino and Suginohara, 1999). Information about all upwelling processes is contained in the thermocline depth, which adjusts to balance the upwelling and descending branches in an equilibrium state (Gnanadesikan, 1999; Schloesser et al., 2012).

Of course, the MOC poleward branch is associated with a zonal, not meridional, pressure gradient. Therefore, the existence of dynamical processes that determine the factor C by linking the meridional with the zonal pressure difference is a precondition for (1) to hold.[1] Several studies point toward the importance of processes along and offshore from the eastern boundary (*e.g.*, Winton, 1996; Marotzke and Scott, 1999; Spall and Pickart, 2001; Pedlosky and Spall, 2005; Cessi and Wolfe, 2009; Spall, 2010; Schloesser et al., 2012).

To explore this issue, Pedlosky and Spall (2005) used a 2-layer model in which a surface buoyancy flux is parameterized by a term (damper) in the continuity equation that relaxes the upper-layer thickness, h_1, to a prescribed value, $H^*(y)$. To represent poleward cooling, H^* decreases monotonically from a value, H_s, in the tropics to lower values ($H^* < H_s$) at higher latitudes. Kelvin waves adjust h_1 to H_s along the eastern boundary but, when Rossby waves attempt to carry that coastal thickness offshore, the damping thins h_1 to H^*, thereby establishing a zonal pressure gradient that drives upper-layer flow poleward in the northeastern ocean.

In an extension of the Pedlosky and Spall (2005) study, Schloesser et al. (2012) used a variable-density, 2-layer model (VLOM), in which a heat flux relaxes upper-layer temperature, T_1, to a prescribed temperature profile, $T^*(y)$, that decreases poleward, reducing to the lower-layer temperature north of a latitude y_2 (as in Eq. (6) below). In this case, Kelvin waves adjust h_1 at the eastern boundary to a profile, $h_e(y)$, such that the depth-integrated, along-shore pressure gradient in layer 1 vanishes. Because that coastal pressure gradient depends on T_1, $h_e(y)$ must thicken polewards, and it increases to the ocean bottom slightly south of y_2 (see Eq. (21)). As in the Pedlosky and Spall (2005) solution, Rossby waves attempt to carry $h_e(y)$ offshore. To damp them, Schloesser et al. (2012) included a detrainment velocity, w_d, in the continuity equation that relaxes h_1 to a prescribed thickness, $h_{\max}$, wherever $h_e(y) > h_{\max}$. (The authors obtained comparable solutions to an OGCM, and argued that w_d in VLOM behaves much like mixing processes in the OGCM.) Consistent with the transports in corresponding OGCM experiments, the MOC strength in VLOM is described by (1), in which the value of f^{-1} is its average over the latitude band where $h_e > h_{\max}$ and

$$C = 1 - \frac{h_{\max}}{D}, \tag{2}$$

where D is the ocean depth.

1.1.2. Wind forcing

While the role of wind forcing in generating upwelling, particularly in the Southern Ocean, has been the focus of many studies, there are only a few studies that directly investigate the impact of wind forcing on the descending branch of the MOC. Tsujino and Suginohara (1999), for example, obtained idealized OGCM solutions in a rectangular basin that extends on either side of the equator; they assumed that the cooling was confined to the southern hemisphere and wind forcing to the northern hemisphere, so that the thermohaline and wind forcings were completely separate. The additional upwelling driven by Ekman suction in the north increased $\mathcal{M}$. Consistent with (1), the thermocline depth increased throughout the basin to allow for the increase in $\mathcal{M}$, a result of basin-wide Kelvin- and Rossby-wave adjustments. Similar solutions were discussed by Klinger et al. (2004).

The upwelling caused by Ekman suction has also been studied using 2-layer models. In the subpolar ocean, where the Ekman pumping velocity is positive ($w_{ek} > 0$), the deep layer can outcrop ($h_1 = 0$) when the winds are sufficiently strong (Huang, 1986; Huang and Flierl, 1987). Within this region, the geostrophic part of the horizontal transport is evenly distributed over the water column, whereas elsewhere in the basin the Sverdrup flow is entirely contained within the upper layer and the deep layer is at rest. In a related study, Nonaka et al. (2006) prevent h_1 from vanishing in regions of Ekman suction by introducing a "mixed-layer" entrainment velocity, w_e, which ensures that h_1 never becomes thinner than a minimum thickness, $h_{\min}$.

The Nonaka et al. (2006) model includes a sponge layer along the northern boundary of the basin, where h_1 is strongly relaxed towards a prescribed value (a representation of the similar sponge layers that exist in many OGCMs). In their steady-state solutions, upwelling in the subpolar ocean is balanced by a convergence of layer-1 water into the sponge layer where it detrains into layer 2, forming a closed overturning cell. Although not noted by the authors, their solutions therefore provide a dynamical explanation for the strengthened MOC in the OGCM solutions of Tsujino and Suginohara (1999) and Klinger et al. (2004). Similarly, Luyten and Stommel (1986) and Radko and Kamenkovich (2011) analyzed solutions to a $2\frac{1}{2}$-layer model, in which surface cooling is represented by a prescribed downwelling velocity from the surface into the second layer and upper-ocean convergence is externally prescribed. Just how the model can generate such a downwelling internally cannot be assessed by their approach, and remains to be understood.

1.2. Present research

In this paper, we extend the MOC study of Schloesser et al. (2012) to include both buoyancy and wind forcing. Our focus is to understand how wind-driven circulations impact the convergence of the MOC surface branch into the northern ocean. Much of the paper concerns the derivation and analysis of quasi-analytic solutions to VLOM. (The solution for western-boundary response must be obtained numerically.) These solutions allow the effects of density and wind forcing to be readily distinguished. To validate and extend the VLOM results, we also obtain solutions to an OGCM (MITgcm), which solves a more accurate set of equations.

Several simplifications to our experimental design are needed to allow for quasi-analytic, VLOM solutions. First, VLOM contains no process corresponding to vertical diffusion in the interior ocean. As a result, the model MOC is not closed by upwelling within the

---

[1] The previous statement assumes that the meridional flow is geostrophic. In zonally-averaged and box models, viscosity (Raleigh damping) has been used to link zonal and meridional flow (Stommel, 1961; Wright and Stocker, 1991; Wright et al., 1998); however, this ageostrophic linkage was shown to be inconsistent with the circulation in more realistic models (Straub, 1996).

domain but rather by allowing flow across an open southern boundary, specifically by regarding either H_s or $\mathcal{M}$ to be an externally prescribed parameter. For our purposes, the lack of interior upwelling is acceptable, since we are interested in understanding the dynamics of the MOC descending branch, which do not explicitly involve the processes that determine the MOC upwelling branch (*e.g.*, Ekman drift out of the Southern Ocean). Second, density is independent of salinity in our idealized experiments; furthermore, solutions are obtained in the limit of very strong surface temperature relaxation, thereby fixing the surface density field to a prescribed value and eliminating any impact of density advection. Both salinity and density advection are known to be important in simulations of MOC variability (*e.g.*, Stommel, 1961; Bryan, 1986; Marotzke and Willebrand, 1991; Winton, 1996). Their neglect in our solutions is acceptable because we explore the dynamics underlying the MOC mean state, not its variability. (In Section 6.5, we report a few OGCM solutions in which density advection is active.) Finally, several simplifications of a mathematical nature are needed to obtain the the VLOM solutions, mostly concerning the western-boundary response; they are noted at the location where they are required in derivations.

Key results are the following. The VLOM solutions provide the complete three-dimensional structure of the flow field, including thermal-wind circulation, and they compare very well to their OGCM counterparts. The dynamics of upper-ocean convergence into the northern ocean change markedly depending on whether the wind-driven Subpolar Gyre extends into the coldest part of the basin: If it does not, the convergence is driven entirely by eastern-boundary adjustments and Rossby-wave damping, as in the Pedlosky and Spall (2005) and Schloesser et al. (2012) studies (Section 7.1); if it does, the convergence rate is also (in some cases entirely) determined by northward, wind-driven flow in the interior of the Subpolar Gyre (Section 5.1). The theory provides two different measures for the strength of the overturning: the rate of deep-water formation, $\mathcal{M}_n$, and the rate of deep-water export from the subpolar ocean, $\mathcal{M}$ (Section 5); the two measures differ because upwelling in the interior subpolar ocean (Nonaka et al., 2006) and in the western-boundary layer provide "shortcuts" for the larger-scale MOC. The theory also provides expressions that relate $\mathcal{M}$ and $\mathcal{M}_n$ to wind amplitude τ_o, $\Delta\rho$, and H_s. Thus, relationships like (1) can be derived, with C changed from (2) to take wind forcing into account.

The paper is organized as follows. First, we describe our layer model, VLOM, and the experimental design in Section 2. We then derive solutions without (Section 3) and with (Section 4) detrainment w_d, and obtain expressions for overturning transports in VLOM (Section 5). To demonstrate the robustness of our results, we compare our VLOM solutions to MITgcm solutions in Section 6, and discuss applications of our VLOM solutions in Section 7. Finally, a summary and discussion is provided in Section 8.

2. The layer model

Here, we present our overall experimental design (Section 2.1), discuss the general VLOM equations for the depth-averaged flow in each layer and their simplifications in the interior ocean and western-boundary layer (Section 2.2), and note that there are also *z*-dependent flows within layer 1 (Section 2.3). The model is very similar to the one used in Schloesser et al. (2012), the main differences being that the present version includes wind forcing, neglects interior diffusion, and the MOC upwelling branch is located outside the model domain. For simplicity, we use a *β*-plane notation in the derivation of our solutions (*i.e.*, we use Cartesian coordinates and neglect terms of order β_y), whereas particular solutions are evaluated on a sphere to allow for better comparison

to our OGCM experiments in Section 6. Solutions depend on several parameters, and the specific values given below are those used in our standard solution.

2.1. Experimental design

The model domain is a rectangular basin representing the North Atlantic that extends meridionally from y_s = 10°N to y_n = 60°N, zonally from x_w = 0°E to x_e = 40°E (see Fig. 2 below), and has a flat bottom at a depth D = 4000 m. Closed conditions are imposed at all boundaries except for the southern boundary, which is open.

The open southern boundary allows information to enter the basin along the eastern boundary via the propagation of Kelvin waves, thereby setting the upper-layer thickness in the southeast corner of the basin to

$$h_1(x_e, y_s) = H_s. \tag{3}$$

In steady state, water flows across y_s only in a western-boundary current. (There is no flow anywhere in the interior of the basin south of y_{1w} = 15°N because there is no interior diffusion or forcing there; see Fig. 1.) Its upper-layer transport is $\mathcal{M}$, the strength of the large-scale MOC (Section 5), and to conserve mass the lower-layer transport is $-\mathcal{M}$. Because H_s and $\mathcal{M}$ are linked by dynamical adjustments within the basin (Section 3), only one or the other must be externally prescribed. In Sections 3 and 4, we treat H_s as an external parameter because the derivation of solutions is more straightforward, commenting on how to obtain solutions with $\mathcal{M}$ specified in Section 7.2. For comparison, in solutions in which all upwelling processes occur within a closed basin, H_s and $\mathcal{M}$ are *both* determined internally by the requirement that the upwelling and sinking branches balance in equilibrium (*e.g.*, Gnanadesikan, 1999; Schloesser, 2011, 2012).

For simplicity, salinity is kept constant and density is assumed to depend only on temperature according to

$$\rho = \rho_o(1 - \alpha T), \tag{4}$$

where ρ_o = 1028 kg/m³ is a background density and α = 0.00015 °C^{-1} is the coefficient of thermal expansion. Thus, there is a one-to-one correspondence between density and temperature, and the two variables can be viewed as being interchangeable. In this regard, subscripts and superscripts are used consistently for the two variables, for example, so that T_1, T_s, T^* implicitly define the corresponding densities $\rho_1 \equiv \rho(T_1)$, $\rho_s \equiv \rho(T_s)$, and $\rho^* \equiv \rho(T^*)$.
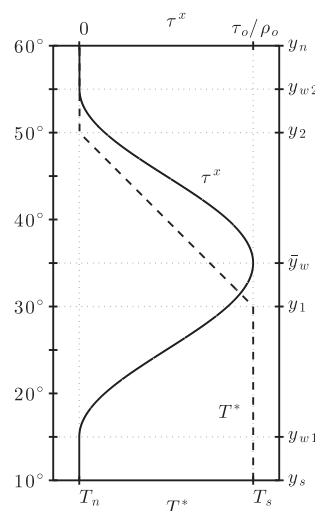

Fig. 1. Meridional profiles of the zonal windstress, $\tau^x(y)$, and the surface relaxation temperature, $T^*(y)$, used in our standard solution.

The model is forced by a heat (buoyancy) flux spread uniformly throughout layer 1. It has the form

$$Q(x,y) = -\frac{T_1 - T^*(x,y)}{\delta t}, \tag{5}$$

where

$$T^*(y) = \begin{cases} T_s, & y \leqslant y_1, \\ T_s + (T_n - T_s)\frac{y-y_1}{y_2-y_1}, & y_1 < y \leqslant y_2, \\ T_n, & y > y_2, \end{cases} \tag{6}$$

δt is a relaxation time that measures the strength of the heating, T_s = 23 °C, T_n = 3 °C, y_1 = 30°N, and y_2 = 50°N (compare Fig. 1). To allow for analytic solutions, we let $\delta t \to 0$ so that $T_1 = T^*(y)$ always. The deep-ocean temperature is everywhere set to $T_2 = T_n$, the temperature of the densest water formed at the surface. Thus, the model ocean is unstratified in the region north of y_2.

The westerly wind stress applied on our model ocean is also shown in Fig. 1, and has the form

$$\tau^x = \frac{1}{2}\frac{\tau_o}{\rho_o}\left[\cos\left(2\pi\frac{y-\bar{y}_w}{y_{w2}-y_{w1}}\right) + 1\right]\theta(y-y_{w1})\theta(y_{w2}-y), \tag{7}$$

where y_{w1} = 15°N, y_{w2} = 55°N, $\bar{y}_w = (y_{w1}+y_{w2})/2$, $\tau_o > 0$, and $\theta(x)$ is a stepfunction (*i.e.*, $\theta(x) = 1$ for $x \geqslant 0$, and $\theta(x) = 0$ for $x < 0$). It drives Subpolar and Subtropical Gyres north and south of $\bar{y}_w$, respectively. We note that the MOC structure in our solutions changes markedly depending on whether the Subpolar Gyre extends into the unstratified part of the ocean (*i.e.*, whether $y_{2w} \gtrless y_2$; see Section 7).

2.2. Equations of motion

2.2.1. General equations

In the stratified part of the ocean ($y \leqslant y_2$), VLOM is a 2-layer system. South of y_2, horizontal transports and layer thickness are described by the equations

$$f\mathbf{k} \times \mathbf{V}_i = -\langle\nabla p_i\rangle + \delta_{i1}\boldsymbol{\tau} + [\nabla \cdot v_h\nabla\mathbf{V}_i], \tag{8a}$$

$$h_{it} + \nabla \cdot \mathbf{V}_i = (-1)^{i-1}w_1, \tag{8b}$$

where subscript i = 1, 2 is a layer index, $\mathbf{V}_i = (h_i\bar{u}_i, h_i\bar{v}_i)$ is the depth-integrated layer transport per unit width in layer i, $\bar{\mathbf{v}}_i = (\bar{u}_i, \bar{v}_i)$ is the depth-averaged velocity, w_1 is the across-interface velocity at the bottom of layer 1, and $\boldsymbol{\tau} = (\tau^x, 0)$ is the surface wind stress divided by ρ_1 (bottom stress is ignored). The depth-integrated pressure gradients in each layer are

$$\langle\nabla p_1\rangle = \frac{gh_1}{\rho_o}\left[\rho_1\nabla(h_1+h_2) + \frac{h_1}{2}\nabla\rho_1\right], \tag{9a}$$

$$\langle\nabla p_2\rangle = \frac{gh_2}{\rho_o}[\rho_2\nabla(h_1+h_2) - \rho_{21}\nabla h_1 + h_1\nabla\rho_1], \tag{9b}$$

where the depth-integrated value of a variable is denoted by $\langle\ldots\rangle$ and $\rho_{21} = \rho_2 - \rho_1$. Mathematical symbols are the horizontal-gradient operator $\nabla \equiv (\partial_x, \partial_y)$, unit vector in the z-direction $\mathbf{k}$, and the Kronecker delta symbol δ_{ij} (δ_{11} = 1 and δ_{21} = 0). The horizontal viscosity term in (8a) is enclosed in brackets to indicate that it is included only formally to allow for a frictional western-boundary layer, but is otherwise unused. Although we obtain steady-state solutions, it is useful to consider how the ocean spins up to equilibrium, so we retain h_{it} in (8b), thereby allowing for Rossby-wave propagation.

The across-interface velocity, $w_1 = w_e + w_c + w_d$, regulates the mass transfer from one layer into the other. Its components are given by

$$w_e = \frac{h_{\min} - h_1}{t_e}\theta(h_{\min} - h_1), \tag{10a}$$

$$w_d = -\frac{h_1 - h_{\max}}{t_d}\theta(h_1 - h_{\max}), \tag{10b}$$

$$w_c = -V_1(y_2)\delta(y - y_2), \tag{10c}$$

where δ is a Dirac delta-function. Velocity $w_e \geqslant 0$ simulates entrainment into a surface "mixed layer" of thickness $h_{\min}$ = 100 m. In order to derive analytical solutions for VLOM, we assume that $t_e \to 0$, which ensures that $h_1 \geqslant h_{\min}$. Velocity $w_d \leqslant 0$ is a detrainment velocity that occurs whenever h_1 becomes thicker than a prescribed maximum value $h_{\max}$ = $3H_s$. It represents processes in the ocean that tend to restratify the water column (*e.g.*, Fox-Kemper et al., 2008), and hence to damp Rossby waves, and it is essential for generating an MOC in solutions without wind forcing (Section 7; Schloesser et al., 2012). To allow for an analytic solution when $w_d \neq 0$, we assume that $t_d \to 0$, in which case w_d acts to ensure that $h_1 \leqslant h_{\max}$ almost everywhere in the basin; the exception is along the eastern boundary, where we assume the time scale for the adjustment by coastal Kelvin waves is much less than t_d (Section 4; Schloesser et al., 2012).

Velocity w_c is a special across-interface velocity that occurs when water flows across y_2. Layer 1 exists just south of y_2 but not just north of it, so that it has a "sidewall" there. Thus, northward flow across y_2 causes layer-1 water to detrain into layer 2, and southward flow across y_2 causes layer-2 water to entrain into layer 1. As such, w_c is conceptually useful for matching the 2-layer and 1-layer regions of the model.

Schloesser et al. (2012) included another across-interface velocity, $w_m = (\kappa/h_1)\theta(D - h_1)$, to represent vertical diffusion in the interior ocean that tends to thicken the thermocline. This process is of secondary importance in our model, since our open southern boundary allows the MOC upwelling branch to occur external to the basin. For simplicity, then, we neglect it altogether.

2.2.2. Interior-ocean equations

It is possible to separate solutions into barotropic and baroclinic parts. We assume that the barotropic flow is in a quasi-steady state ($h_{1t} + h_{2t} = 0$ in Eq. (8b)), a reasonable assumption since barotropic waves propagate so much faster than baroclinic ones. In the interior ocean where viscosity is neglected, the sums of (8) and (9) then give

$$f\mathbf{k} \times \mathbf{V} = -\nabla P + \boldsymbol{\tau}, \qquad \nabla \cdot \mathbf{V} = 0, \tag{11a}$$

$$\nabla P = \langle\nabla p_1\rangle + \langle\nabla p_2\rangle = \frac{g}{2\rho_o}\nabla\left(\rho_1 h^2 + \rho_{21}h_2^2\right), \tag{11b}$$

where $\mathbf{V} = \mathbf{V}_1 + \mathbf{V}_2$ and $h = h_1 + h_2$.

Since ∇P is a perfect differential, Eq. (11a) give the depth-integrated, Sverdrup transports and transport streamfunction (defined by $U = -\Psi_y$ and $V = \Psi_x$),

$$U = -\frac{1}{\beta}\tau_{yy}^x(x_e - x), \qquad V = -\frac{1}{\beta}\tau_y^x, \qquad \Psi = \frac{1}{\beta}\tau_y^x(x_e - x), \tag{12}$$

where the boundary condition $U(x_e) = \Psi(x_e) = 0$ is applied at the eastern boundary. With Ψ known, the sea-surface slope, ∇h, obtained by substituting (11b) into (11a), is

$$g\nabla h = -\frac{g}{2\rho_o}D\nabla\rho_1 - \frac{1}{2D}\nabla\left(g'h_2^2\right) + \frac{1}{D}(\boldsymbol{\tau} + f\nabla\Psi), \tag{13}$$

where $g' \equiv g(\rho_2 - \rho_1)/\rho_2$, and $h_1 + h_2 \approx D$ and $|\rho_i - \rho_j| \ll \rho_i$ with i, j = 0, 1, 2 are assumed. Expression (13) is a statement that the sea-surface-height gradient consists of baroclinic (first two terms) and barotropic (the last term) contributions. Eqs. (12) and (13) also describe the solution in the northern, unstratified region north of y_2, where h_1 vanishes, and the wind forcing acts directly on layer 2.

Using (13) to eliminate ∇h, the pressure gradient terms in layers 1 and 2 (Eqs. (9)) can be rewritten entirely in terms of h_1 to get

$$\langle\nabla p_1\rangle = \frac{D-h_1}{D}\nabla\left(\frac{1}{2}g'h_1^2\right) + \frac{h_1}{D}(\boldsymbol{\tau} + f\nabla\Psi), \tag{14a}$$

$$\langle\nabla p_2\rangle = -\frac{D-h_1}{D}\left[\nabla\left(\frac{1}{2}g'h_1^2\right) - (\boldsymbol{\tau} + f\nabla\Psi)\right], \tag{14b}$$

where the first terms are associated with the baroclinic shear, and the second terms with the depth-integrated geostrophic flow, respectively. After inserting (14a) into (8a) and neglecting viscosity, the layer-1 equations in (8) are a set of three equations with three unknowns. It is the set solved in Sections 3–7 to obtain the baroclinic part of the response in the interior ocean.

2.2.3. Western-boundary equations

The interior circulation is closed in a western-boundary layer. For the purpose of studying the MOC, it is sufficient to know only its zonally integrated properties, rather than details of its across-shore structure. Specifically, we solve for the meridional layer transports, $\mathcal{V}_{iw}(y) \equiv \int_{x_w}^{x_w^+} V_i \, dx$, $i = 1, 2$, and the zonally-integrated upwelling into layer 1, $W_w(y) \equiv \int_{x_w}^{x_w^+} w_1 \, dx$, where x_w^+ is the eastern edge of the boundary layer. As discussed below, the set of equations that determine these quantities also involves knowing the layer-1 thickness at the western boundary, $h_w(y) \equiv h_1(x_w, y)$. The equations rely on several approximations. One of them is the usual restriction that the boundary layer is narrow enough so that we can take the limit $x_w^+ \to x_w$, thereby eliminating the boundary-layer width from the solution.

To conserve mass, the depth-integrated meridional transport $\mathcal{V}_w(y) \equiv \mathcal{V}_{1w} + \mathcal{V}_{2w}$ has to be opposite to the zonally-integrated interior flow given by (12). Zonal integration of the interior flow then yields

$$\mathcal{V}_w = \int_{x_w}^{x_w^+} V \, dx = -\int_{x_w^+}^{x_e} V \, dx = \frac{1}{\beta} \tau_y^x (x_e - x_w), \quad (15)$$

where the narrowness of the current allows x_w^+ to be replaced by x_w in the last term.

To obtain $\mathcal{V}_{1w}(y)$, we integrate the layer-1 continuity equation across the boundary layer and equatorward from y_2, because Kelvin waves propagate in that direction along a western boundary. The resulting expression is

$$\mathcal{V}_{1w}(y) = -\int_{y_2^-}^{y_2} W_w \, dy' - \int_{y}^{y_2^-} W_w \, dy' + \int_{y}^{y_2} U_{1w}^+ \, dy', y \leqslant y_2, \quad (16)$$

where $U_{1w}^+ \equiv U_1(x_w^+)$ is the zonal transport/width in the interior solution that flows into or out of the boundary layer across $x = x_w^+$, and $y_2^- = y_2 - \delta$, $\delta \to 0$, is a latitude just south of y_2. For completeness, we note that $\mathcal{V}_{1w}(y) = 0$ for $y > y_2$ since layer 1 does not exist there. As discussed next, the W_w integral in (16) is split into two parts in order to separate out the impact of w_c.

North of y_2 where the ocean is unstratified, the southward western-boundary transport $\mathcal{V}_w$ has no baroclinic structure. As it flows across y_2, Q heats the upper part ($z > -h_{\min}$) of the flow to a temperature $T^* > T_n$, forming a layer 1 of thickness $h_{\min}$ and setting $\mathcal{V}_{1w}(y_2) = (h_{\min}/D)\mathcal{V}_w(y_2)$. From the definition of w_c, it follows that

$$-\int_{y_2^-}^{y_2} W_w \, dy' = -\int_{y_2^-}^{y_2} \int_{x_w}^{x_w^+} w_c \, dy' = \mathcal{V}_{1w}(y_2) = \frac{h_{\min}}{D} \mathcal{V}_w(y_2), \quad (17a)$$

a statement that water shallower than $z = -h_{\min}$ that flows southward across y_2 is instantly entrained into layer 1.

South of y_2, the only component of w_1 that impacts the western-boundary layer is w_e, which is given by (10a) in the limit that $t_e \to 0$. (In all our solutions, $w_d = 0$ in the western-boundary layer because $h_1 < h_{\max}$ there.) Since $h_w^+(y) \equiv h_1(x_w^+, y) \geqslant h_{\min}$, and assuming that h_1 varies monotonically across the boundary layer, $w_e \neq 0$ only where h_w attains its minimum value $h_{\min}$ and where there is a net divergence of the layer-1 flow across the current. The zonally-integrated continuity equation then gives

$$W_w(y) = \begin{cases} \mathcal{D}\theta(\mathcal{D})\theta(y - \bar{y}_w), & h_w = h_{\min}, \\ 0, & h_w > h_{\min}, \end{cases} \quad y < y_2, \quad (17b)$$

where $\mathcal{D}(y) = \mathcal{V}_{1wy} + U_{1w}^+$. An additional factor of $\theta(y - \bar{y}_w)$ is included in (17b). It ensures that $W_w = 0$ everywhere in the subtropics ($y < \bar{y}_w$). This neglect is consistent with our OGCM solutions, for which there is never any western-boundary upwelling in the subtropics. It is also required to avoid inaccuracies that result from the closure discussed below.

As assumed in (17b), h_1 does vary monotonically across the western-boundary layer if the horizontal viscosity has the form of Raleigh damping (Stommel, 1948). On the other hand, it does not vary monotonically for Laplacian horizontal viscosity, since the boundary-layer structure oscillates as well as decays offshore (Munk, 1950). The minimum value of h_1 still occurs at $x = x_w$ when the boundary current has northward shear ($h_w < h_w^+$), however, a minimum also occurs offshore, at the longitude of the first over-shooting, for southward shear ($h_w > h_w^+$). Thus, (17b) neglects contributions to W_w in the latter case. This error, however, is small because of the Munk layer's offshore decay.

A final western-boundary equation is required relating $\mathcal{V}_{1w}$ to h_w, either to calculate h_w when $W_w = 0$, or $\mathcal{V}_{1w}$ when $h_w = h_{\min}$ and $W_w \neq 0$. To obtain that expression, we adopt the typical boundary-layer assumption that the alongshore flow is geostrophic. The zonal pressure gradient is given by (14a), and a zonal integration of the geostrophic balance in (8a) gives

$$\mathcal{V}_{1w}(y) = \frac{g'}{2f}\left[h_w^{+2} - h_w^2 - \frac{2}{3D}\left(h_w^{+3} - h_w^3\right)\right] + \int_{x_w}^{x_w^+} \frac{h_1}{D} V_w \, dx. \quad (18a)$$

(The across-current integral of τ^x is negligible in Eq. (18a) in the limit that $x_w^+ \to x_w$.)

The last term in (18a) depends on the structure of the boundary layer. Since we wish to avoid having to calculate that structure, a closure is required. We choose

$$\int_{x_w}^{x_w^+} \frac{h_1}{D} V_w \, dx = \frac{h_w}{D} \mathcal{V}_w. \quad (18b)$$

This simple closure is particularly accurate in regions where western-boundary upwelling occurs ($W_w > 0$), that is in the subpolar region where either $h_w^+ = h_{\min}$ (in the center of the Subpolar Gyre) or $V_w \approx 0$ (near the gyre boundary $\bar{y}_w$; see Section 3.3). It is less accurate in regions where h_w^+ is large and h_1 varies considerably across the boundary layer (i.e., in the subtropics); because $W_w = 0$ there, such that (18) is only used to calculate $h_w(y)$ (a result without interest in our study), the closure's accuracy is irrelevant in that region.[2]

To summarize, Eqs. (16)–(18) involve the quantities, h_w^+ and U_{1w}^+, which either are known from the interior solution or are specified externally in the region covered by Rossby waves emanating from the western boundary. Thus, they provide a set of three independent equations in the three unknowns, $\mathcal{V}_{1w}, W_w$, and h_w. Section 3.3 describes a numerical algorithm for obtaining a solution to this set of equations. With $\mathcal{V}_{1w}$ known, $\mathcal{V}_{2w} = \mathcal{V}_w - \mathcal{V}_{1w}$, to complete the western-boundary solution.

2.3. Depth-dependent currents

2.3.1. Overview

The above discussion concerns the depth-integrated currents within each layer. The layer-1 currents, however, vary with z, owing to the presence of the wind-driven Ekman layer and thermal-wind shear. Because we neglect density advection, the depth-integrated flow $\bar{\mathbf{v}}_1$ is independent of the z-dependent (shear) part,

---

[2] In principle, a more accurate closure will ensure that $W_w = 0$ in the subtropics without the need for the "artificial" stepfunction in (17b). We have explored other, more accurate closures but the resulting increase in complexity is unwarranted for our purposes. Also note that if the stepfunction in (17b) were eliminated, the entrainment in the subtropics would still be small relative to the overturning strength in our standard solution.

$\mathbf{v}_s = \mathbf{v}_1 - \bar{\mathbf{v}}_1$. Thus, including $\mathbf{v}_s$ is not essential for obtaining solutions. Nevertheless, obtaining the full, 3-dimensional flow field is useful for discussing where water sinks in solutions, and it allows VLOM solutions to be more closely compared to corresponding OGCM experiments (see Schloesser, 2011; Schloesser et al., 2012).

2.3.2. Interior-ocean currents

In the interior ocean, where viscosity is negligible, the complete $\mathbf{v}_1$ field is

$$u_1 = \frac{U_1}{h_1} - \frac{g'_y}{f}\left(z + \frac{h_1}{2}\right), \qquad v_1 = \frac{V_1}{h_1} - \frac{\tau^x}{f}\left[\delta(z) - \frac{1}{h_1}\right], \tag{19a}$$

where the last terms in u_1 and v_1 are the shear parts of the thermal wind and the infinitesimally thin Ekman layer, respectively. (The depth-integrated parts of the thermal wind and Ekman flow are included in U_1 and V_1.) With the aid of (19a), the vertical velocity within the upper layer ($z \geqslant -h_1$) follows from a z-integration of the continuity equation and imposition of the boundary condition that $w = 0$ at $z = 0$, yielding

$$w = -\int_0^z (u_{1x} + v_{1y})dz = w_{ek}\left[1 - \theta(z) + \frac{z}{h_1}\right] - w_1\frac{z}{h_1}, \quad z > -h_1, \tag{19b}$$

where $w_{ek} \equiv -(\tau^x/f)_y$ is the Ekman-pumping velocity and $\theta(z) = 1$ for $z \geqslant 0$ and $\theta(z) = 0$ otherwise. Similarly, the complete $\mathbf{v}_2$ field is

$$u_2 = \frac{U_2}{h_2}, \qquad v_2 = \frac{V_2}{h_2} - \frac{\tau^x}{f}\left[\delta(z) - \frac{1}{D}\right]\theta(y - y_2). \tag{19c}$$

The term proportional to $\theta(y - y_2)$ in (19c) reflects the property that the wind acts in layer 2 north of y_2 where there is no layer 1. The w field in layer 2 is then

$$w = \int_{-D}^z (u_{2x} + v_{2y})dz$$
$$= w_{ek}\left[1 - \theta(z) + \frac{z}{D}\right]\theta(y - y_2) + w_1\frac{z + D}{h_2}\theta(y_2 - y), \qquad z \leqslant -h_1, \tag{19d}$$

the last term active only south of y_2 where layer 1 exists, and the first term north of y_2, where layer 2 is directly forced by the wind.

Along the eastern and western boundaries, u_1 must vanish. The depth-averaged flow $\bar{u}_1 = U_1/h_1$ is brought to zero by the dynamical processes discussed in Section 3. Boundary layers are needed to ensure that $u_s = 0$ as well, and water sinks or rises to close the shear circulation within them (see Schloesser et al., 2012).

3. Standard solution

In this section, we derive and discuss our standard VLOM solution. It assumes that $w_d = 0$ so that the only process that allows water to detrain from layer 1 to layer 2 is w_c, that is, detrainment occurs only across the sidewall of layer 1 at $y = y_2$. It also assumes that $y_2 < y_{2w}$, which ensures that the Subpolar Gyre extends into the region where the model consists of a single layer. We begin with a description of the spin-up of the response (Section 3.1), which serves both to provide an overview of the solution and to highlight the underlying physics. Next, we obtain the steady-state flow field in the interior ocean (Section 3.2) and along the western boundary (Section 3.3). We conclude by discussing the impacts of including the shear flow within layer 1 (Section 3.4).

3.1. Spin-up and overview

Let the initial state of the model be a state of rest with $h_1 = H_s$ everywhere. Barotropic waves quickly adjust the depth-integrated circulation to Sverdrup balance (12), which for forcing (7) consists of Subtropical and Subpolar Gyres. Substituting (12) and (14) with $h_1 = H_s$ into (8), gives the interior-ocean transports in each layer at this adjustment stage,

$$U_1 = -\frac{D - H_s}{D}\frac{g'_y}{2f}H_s^2 - \frac{H_s}{D}\frac{\tau^x_{yy}}{\beta}(x_e - x), \qquad V_1 = -\frac{\tau^x}{f} + \frac{H_s}{D}\frac{f}{\beta}w_{ek}, \tag{20a}$$

$$U_2 = \frac{D - H_s}{D}\frac{g'_y}{2f}H_s^2 - \frac{D - H_s}{D}\frac{\tau^x_{yy}}{\beta}(x_e - x), \qquad V_2 = \frac{D - H_s}{D}\frac{f}{\beta}w_{ek}. \tag{20b}$$

Note that Eqs. (20) include depth-integrated flows from three components: the geostrophic part of the Sverdrup flow, thermal-wind shear, and Ekman transport.

At the eastern boundary ($x = x_e$), the wind-driven component of U_1 vanishes in (20), but the thermally-driven part (proportional to g'_y) does not. As a result, in the latitude band where $g'_y < 0$ $\left(T^*_y < 0\right)$, the thermally-driven flow converges in layer 1 and diverges in layer 2 there, and h_1 thickens. The thickening continues until the passage of coastal Kelvin waves, which adjusts the eastern-boundary layer thickness $h_1(x_e, y)$ to a profile $h_e(y)$ in which the depth-averaged, meridional pressure gradient $\langle p_{1y}\rangle$, and hence $U_1(x_e, y)$, vanish. With the aid of (14a), $\langle p_{1y}\rangle = 0$ implies that $\left(g'h_1^2\right)_y = 0$ since $\psi = 0$ at the eastern boundary. Together with boundary condition (3), it follows that

$$h_e(y) = \begin{cases} H_s\left(\frac{g'_s}{g'}\right)^{1/2}, & y < y', \\ D, & y \geqslant y', \end{cases} \tag{21}$$

where $g'_s = g'(y_s)$. According to (21), h_e increases northward as g' decreases, and y' is the latitude where it first reaches the bottom; that is, y' is defined by $g'(y')/g'_s = H_s^2/D^2$ (see the top panels of Fig. 6 below). Because Kelvin waves propagate so rapidly, this adjustment happens within the first year of the spin-up. Note that since τ^x does not affect $\langle p_{iy}\rangle$, (21) is the same as in solutions without wind forcing (Schloesser et al., 2012).

In the interior ocean, Ekman pumping begins to thicken and thin h_1 in the subtropical and subpolar ocean, respectively. At the same time, baroclinic Rossby waves propagate away from the eastern boundary. After their passage, h_1 is adjusted to an equilibrium state in which Ekman convergence and divergence is balanced by geostrophic flow. These processes are described by

$$h_{1t} + \mathbf{c}_r \cdot \nabla h_1 = -\frac{D - h_1}{D}w_{ek} + w_1, \tag{22a}$$

with

$$\mathbf{c}_r = (c_r^x, c_r^y)$$
$$= \left[-\beta\frac{D - h_1}{D}\frac{g'h_1}{f^2} + \frac{h_1^2 g'_y}{2Df} - \frac{\tau^x_{yy}}{D\beta}(x_e - x)\right]\mathbf{i} + \left(\frac{1}{D}\frac{f}{\beta}w_{ek}\right)\mathbf{j}, \tag{22b}$$

obtained by eliminating $\mathbf{v}_1$ in the inviscid version of (8). According to (22a), baroclinic Rossby waves propagate boundary values of h_1 into the interior ocean along characteristic curves, $[x_r(s), y_r(s)]$, defined by integrations of $dx_r/ds = c_r^x$ and $dy_r/ds = c_r^y$ (see Eq. (28) below), and they are altered by wind forcing and mixing (the terms on the right-hand side). For example, the eastern-coastal profile $h_e(y)$ is carried westward by Rossby waves along characteristics, thinning in regions where $w_{ek} > 0$ (Subpolar Gyre) and thickening where $w_{ek} < 0$ (Subtropical Gyre). Note also that $\mathbf{c}_r$ is not oriented due westward because it is impacted by the forcing, both by wind (Young, 1981; Luyten et al., 1983; Rhines, 1986) and T^*_y (Schloesser et al., 2012). Fig. 2 plots characteristic curves for our standard run (black and

white curves), and their deviation from westward orientation is apparent.

For weak winds, $h_1 > h_{min}$ and eastern-boundary characteristics fill the entire basin (Region A in Fig. 2 extends to the western boundary). For sufficiently strong winds, however, these properties break down: (1) h_1 can thin to h_{min} in a western region of the sub-polar ocean (Region B_1 in Fig. 2); and (2) c_r^x can become positive, so that baroclinic Rossby waves propagate *eastward*, in a region where the Sverdrup flow has an eastward component ($\tau_{yy}^x < 0$; west of the orange curve in Fig. 2). Because of (2), there is a region in the domain that is filled by Rossby-wave characteristics that emerge from the *western* boundary (Region B_2 in Fig. 2). The nature of the solution in Region B_2 is fundamentally different from that in Regions A and B_1, which are determined by Rossby waves that propagate from the eastern boundary; to put it another way, the western-boundary layer, which otherwise passively closes the interior circulation, now actively affects it. As we shall see, however, the impact of this c_r^x reversal on the large-scale MOC is relatively small in our solutions. It is not necessary that Region B_2 lie inside of Region B_1. In the standard run, although most of Region B_2 does lie within Region B_1, a tiny part, very near its southern edge, lies outside (the red curve in Fig. 2 intersects the western boundary south of the magenta curve; see the discussion at the end of Section 3.2.2.1).

The final stage of the spin-up is the adjustment of the western-boundary currents to the interior circulation. Because western-boundary Kelvin waves propagate southward, they extend to the southern boundary of the basin. Furthermore, since there is no barotropic flow south of y_{w1} for our wind forcing, the two layer transports balance there, with the layer-1 and layer-2 flows corresponding to the MOC upper and deep branches, respectively. It is worth noting that in related closed-basin solutions (Kawase, 1987; Schloesser et al., 2012) the spin-up is not complete at this stage. In these solutions, $h_w(y_s)$ is propagated to the eastern boundary by Kelvin waves along the southern boundary (or the equator if $y_s < 0$) where it resets H_s. Consequently, several series of wave reflections similar to the spin-up described above are required for solutions to reach a steady state.
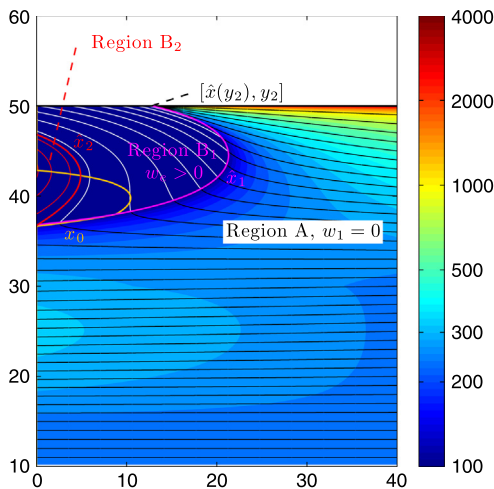

Fig. 2. Map of Rossby-wave characteristics and layer thickness h_1 (shading) in the VLOM standard solution with $H_s = 250$ m and $\tau_o = 0.12$ Nm^{-2}. Black/white curves delineate characteristics starting from the eastern boundary, and red curves those from the western boundary layer. Also indicated are the eastern edge of Region B_2 ($\hat{x}_2(y)$; the easternmost red curve), curve $x_0(y)$ (orange), along which the zonal Rossby-wave speed vanishes, and the eastern edge of Region B_1, $\hat{x}_1(y)$ (magenta curve). (For interpretation of the references to colour in this figure legend, the reader is referred to the web version of this article.)

3.2. Interior ocean

As noted above, solutions to the steady-state version of (22a) are complicated by the possible presence of Regions B_1 and B_2. We proceed by first assuming that Region A exists everywhere in the basin (*i.e.*, $w_1 = 0$ and $c_r^x < 0$ everywhere). Then we modify the solution west of curve $\hat{x}(y) = \max[\hat{x}_1(y), \hat{x}_2(y)]$, where $\hat{x}_1(y)$ and $\hat{x}_2(y)$ are the eastern edges of Regions B_1 and B_2, respectively.

3.2.1. Region A

There are two subregions within Region A where $h_2 \neq 0$ (Region A_1) and $h_2 = 0$ (Region A_2), the two separated by the curve $x_D(y)$ defined below. The solution in Region A_2 is just the barotropic response (12), with h_1 determined by (13) after setting $h_2 = 0$. For typical model parameters, Region A_2 exists only very near y_2. In the standard run, for example, it lies so close to y_2 that it is not visible as a distinct area in Figs. 2 and 3 (darkest-red shading) and is barely visible in the upper panels of Fig. 4, which provides a meridionally expanded view of the solution.

The solution in Region A_1 can be found numerically by integrating the steady-state version of (22a), subject to the eastern-boundary condition that $h_1(x_e, y) = h_e(y)$. On the other hand, it is possible to obtain the solution analytically after first noting that potential-vorticity conservation requires that $\mathbf{v}_2 = 0$ (Luyten et al., 1983). Using the layer-2 equations in (8) with $h_{2t} = w_1 = 0$ and (14b), one can show that

$$\mathbf{\nabla}\left(\frac{h_2}{f}\right) \times \mathbf{\nabla}\psi_2 = 0, \tag{23}$$

where ψ_2 is the layer-2 streamfunction ($U_2 = -\psi_{2y}$, $V_2 = \psi_{2x}$). According to (23), streamlines of the layer-2 flow are parallel to lines of constant h_2/f. Furthermore, setting $h_{1t} = w_1 = 0$ in (22) and using $\mathbf{\nabla}h_1 = -\mathbf{\nabla}h_2$, it is straightforward to show that $\mathbf{c}_r \cdot \mathbf{\nabla}(h_2/f) = 0$, a statement that h_2/f is conserved along Rossby-wave characteristics. Since the entire Region A is covered by eastern-boundary characteristics, *all* isolines of h_2/f intersect the eastern boundary in that region. Because there can be no flow through that solid boundary, it follows that $\psi_2 = \mathbf{v}_2 = 0$ everywhere in Region A.

Since the layer-2 flow is geostrophic in Region A_1, $\mathbf{v}_2 = 0$ implies that $\langle\mathbf{\nabla}p_2\rangle = 0$ as well, and it follows from (14b) that

$$\mathbf{\nabla}\left(\frac{1}{2}g'h_1^2\right) = \boldsymbol{\tau} + f\mathbf{\nabla}\Psi = -\mathbf{\nabla}\left[\frac{f^2}{\beta}w_{ek}(x_e - x)\right]. \tag{24}$$

To determine h_1 at a point (x, y) in Region A_1, we integrate (24) along any pathway within Region A_1 that extends from (x, y) to the eastern boundary (where h_1 is known). A convenient path is from (x, y) to (x_e, y_s), which gives

$$h_1(x, y) = \left[\frac{g_s'}{g'}H_s^2 - \frac{2f^2}{g'\beta}w_{ek}(x_e - x)\right]^{1/2}, \qquad x \leqslant x_D(y). \tag{25}$$

It is useful to backsolve (25) to obtain lines of constant $h_1 = H$ in Region A_1,

$$x_H(y, H) = x_e - \frac{g_s'H_s^2 - g'H^2}{2(f^2/\beta)w_{ek}}. \tag{26}$$

The boundary between Regions A_1 and A_2, $x_D(y)$, is given by (26) with $H = D$.

An interesting feature of (26) along $y = y_2$ is that *all* h_1 contours within the Subpolar Gyre converge to a single point $[x_H(y_2, H), y_2]$. This curious property happens because (26) is *independent* of H when $y = y_2$ since $g'(y_2) = 0$. Provided that τ_o is strong enough or H_s small enough ($\gamma_c \geqslant 1$ defined below), $x_H(y_2, H) > 0$ and lies within the model domain. This property holds for the standard run, and is visible in Fig. 2 by the convergence of all color shadings to the
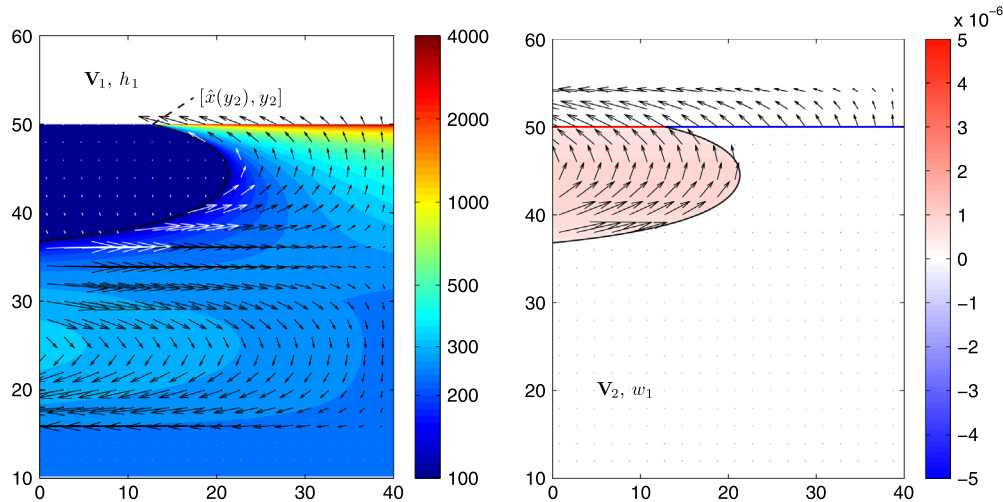
Fig. 3. Maps of the layer thickness h_1 (shading) and the horizontal transports/width $\mathbf{v}_1$ (arrows) in layer 1 (left panel), and the across-interface velocity w_1 (shading) and horizontal transports/width $\mathbf{v}_2$ (arrows) in layer 2 (right panel) in the VLOM standard solution with $H_s = 250$ m and $\tau_o = 0.12$ Nm^{-2}. Detrainment $w_c(y_2) < 0$ is indicated as a blue line to the east of $\hat{x}(y_2)$, and entrainment $w_c(y_2) > 0$ as a red line farther to the west. Corresponding boundary current transports are shown in Fig. 5. (For interpretation of the references to colour in this figure legend, the reader is referred to the web version of this article.)

point $[\hat{x}(y_2), y_2]$. As a result, $h_1(y_2)$ jumps from D at $x > \hat{x}(y_2)$ to h_{min} at $x < \hat{x}(y_2)$.

An expression similar to (26) holds for the characteristic curves in Region A$_1$. Recall that h_2/f is conserved along characteristics. It follows that

$$q \equiv \frac{D - h_1}{f} = \frac{D - h_e(Y)}{f(Y)}, \tag{27}$$

for the characteristic that emerges from the eastern boundary at latitude $y = Y$. Using (27) to eliminate H from (26) yields the curve,

$$x_Y(y, Y) = x_e - \frac{g_s' H_s^2}{2(f^2/\beta)w_{ek}} + \frac{g'}{2(f^2/\beta)w_{ek}} \left\{ D - \frac{f}{f(Y)}[D - h_e(Y)] \right\}^2, \tag{28}$$

for that characteristic. Generally, $x_H(y, H)$ and $x_Y(y, Y)$ are not the same curve, as is evident in Fig. 2, the only exception occurring when $H = D$ and $Y = y'$. (Recall that y' is the latitude where $h_e = D$ occurs first; thus, curve $x_Y(Y = y')$ defines the boundary between Regions A$_1$ and A$_2$).

According to (28), all characteristic curves intersect y_2 at the same focal point as for h_1 contours. In Fig. 2, however, many of them are not able to do so because they first intersect Region B$_1$ south of y_2. Inequality

$$\frac{D - h_e(Y)}{f(Y)} < \frac{D - h_{min}}{f(y_2)}, \tag{29}$$

provides a necessary condition for characteristic $x_Y(x, Y)$ to intersect the focal point. Since q is constant along $x_Y(x, Y)$, (29) ensures that $h_1 > h_{min}$ everywhere along its path, and hence it remains within Region A south of y_2.

With h_1 known everywhere in Region A, the layer-1 flow $\mathbf{v}_1$ can be determined from (8a) and (14a). Since the depth-integrated flow is the Sverdrup circulation (12) and $\mathbf{v}_2 = 0$, $\mathbf{v}_1$ is just (12), i.e., the Sverdrup flow is contained entirely within layer 1. Fig. 3 plots the Region-A flow field, and the Sverdrup Gyres are apparent in layer 1 (left panel).

Since $V_1(y_2) > 0$ within the Subpolar Gyre, layer-1 water flows northward across y_2. It is cooled to T_n as it does, and hence detrains into layer 2 at the rate

$$w_c(x, y_2) = -V_1(y_2) = -\frac{\tau_y^x}{\beta}, \qquad x \geqslant \hat{x}. \tag{30}$$

This detrainment is apparent in Fig. 3 in that the layer-1 Sverdrup flow shifts to layer 2 north of y_2. Thus, flow within the Subpolar Gyre provides another mechanism (other than Rossby-wave damping when $w_d \neq 0$; see Section 4) for the convergence of the MOC surface branch into the northern ocean.

3.2.2. Region B

Although the dynamics that determine the responses in Regions B$_1$ and B$_2$ are distinctly different, the solutions in each region have a similar structure; moreover, we adopt an approximation for the Region-B$_2$ solution that ensures they are the same (see below). It is therefore useful to define the entire area covered by Regions B$_1$ and B$_2$ to be Region B (i.e., $B = B_1 \cup B_2$), such that $\hat{x}(y)$ refers to its eastern edge. In addition, we define latitudes $\hat{y}_s$ and $\hat{y}_n$ to be the southernmost and northernmost latitudes of Region B.

3.2.2.1. Region B$_1$. In the subpolar ocean, Ekman suction ($w_{ek} > 0$) thins h_1 away from the eastern boundary. Depending on the strength of the winds and the value of H_s, h_1 may reach its minimum thickness h_{min} along curve $\hat{x}_1(y)$ in the interior ocean. In that case, $w_1 = w_e$ ensures that $h_1 = h_{min}$ west of $\hat{x}_1$ by transferring mass from layer 2 to layer 1, thereby establishing Region B$_1$. When Region B$_1$ exists, $\hat{x}_1(y)$ is defined by (26) with $H = h_{min}$, that is,

$$\hat{x}_1(y) = x_e - \frac{g_s' H_s^2 - g' h_{min}^2}{2(f^2/\beta)w_{ek}}. \tag{31}$$

For the standard run, Region B$_1$ extends meridionally from latitude $y = 36.8°$N to $\hat{y}_n = y_2$ (Fig. 2, the region west of the magenta curve).

Region B$_1$ exists only if $\hat{x}_1(y) > x_w^+$ for some y, and since $g_s' H_s^2 > g' h_{min}^2$ and $w_{ek} > 0$, (31) implies that H_s must be sufficiently small or w_{ek} sufficiently large. By differentiating $\hat{x}_1$ with respect to y, it is straightforward to show that the maximum value of $\hat{x}_1(y)$ occurs in the Subpolar Gyre at a latitude $y = y_b$ somewhat south of the latitude where $\tau_{yy}^x = 0$, and for the standard run $y_b = 44.5°$N. Eq. (31) implies that Region B$_1$ exists ($\hat{x}_1 > x_e$) only if $H_s < H_b$, where
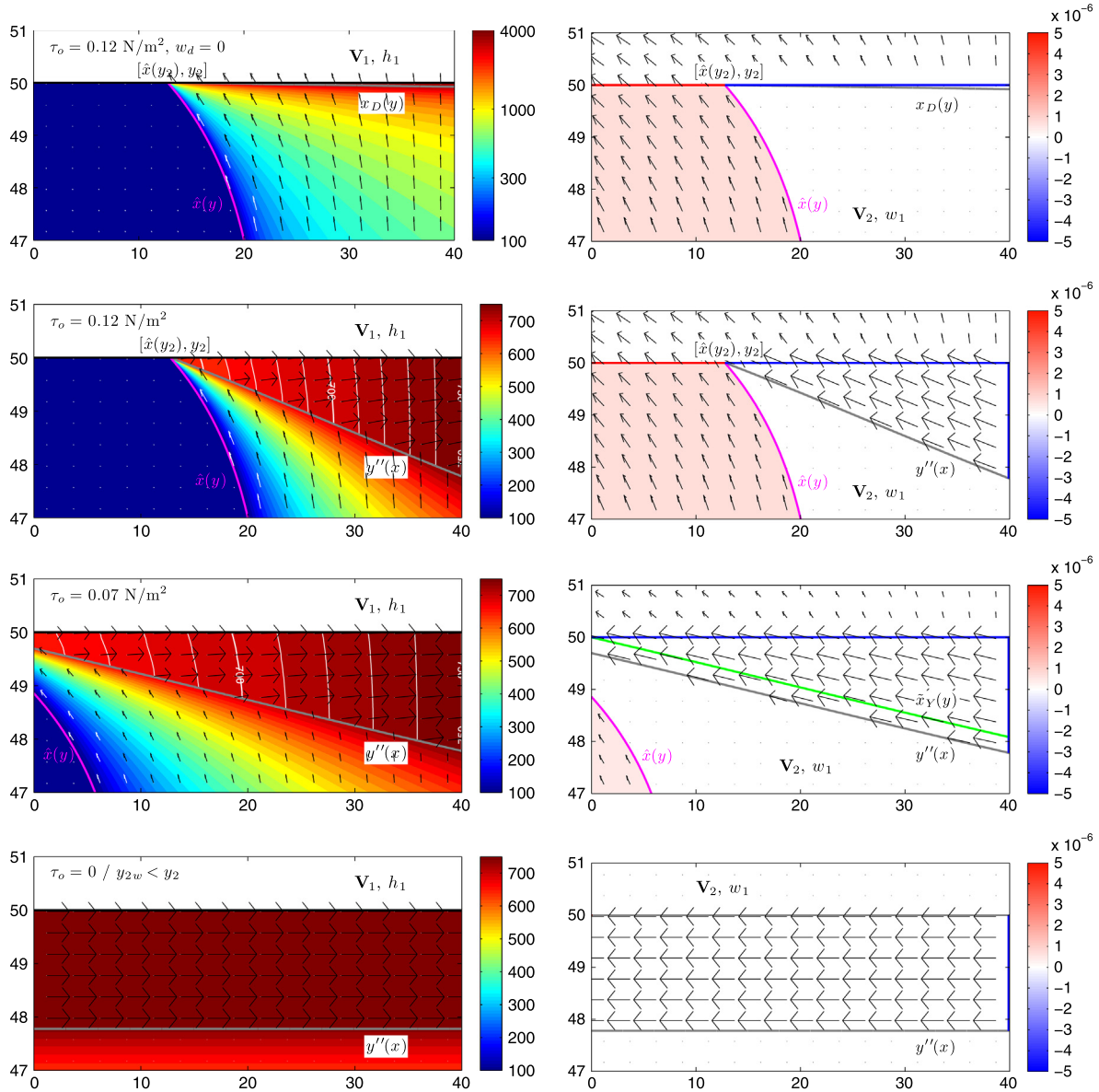
Fig. 4. Maps providing a meridionally enlarged view of upper-layer thickness h_1 (shading and white contours) and layer-1 transports $\mathbf{v}_1$ (arrows) in the left panels and across-interface velocity w_1 (shading) and layer-2 transports $\mathbf{v}_2$ (arrows) in the right panels. Each row corresponds to a different solution. The standard solution is presented in the top panels. The other solutions shown differ from the standard run by having $w_d \neq 0$ (upper-middle panels), $\tau_o = 0.07$ N/m² (lower-middle panels), and $\tau_o = 0$ (bottom panels). Gray curves indicate the either the southern edge of Region A_2 (top panels) or Region N (all other panels). The green curve in the lower-middle right panel marks the characteristic $\tilde{x}_Y(y)$ as defined in Section 5.1.2. Magenta curves show the boundary between Regions A and B, $\hat{x}(y)$. (For interpretation of the references to colour in this figure legend, the reader is referred to the web version of this article.)

$$H_b = \left[\frac{g'}{g'_s} h_{\min}^2 + \frac{2f^2}{g'_s \beta} w_{ek}(x_e - x_w^+) \right]^{1/2}, \qquad y = y_b. \quad (32)$$

The dimensionless parameter,

$$\gamma_b = \frac{H_b^2}{H_s^2}, \quad (33)$$

then indicates whether an outcropping of the deep layer does ($\gamma_b > 1$) or does not occur ($\gamma_b \leqslant 1$).

Solutions also change their properties depending on whether the northern edge of Region B_1 intersects the western or northern boundary. The value of H_s at which $\hat{x}_1$ intersects the corner point (x_w^+, y_2), found by setting $\hat{x}_1 = x_w^+$ and $g'(y_2) = 0$ in (31), is

$$H_c = \left[\frac{2f^2}{g'_s \beta} w_{ek}(x_e - x_w^+) \right]^{1/2}, \qquad y = y_2. \quad (34)$$

The dimensionless parameter,

$$\gamma_c = \frac{H_c^2}{H_s^2}, \quad (35)$$

then determines whether h_1 contours intersect the western boundary ($\gamma_c \leqslant 1$) or latitude $y_2 (\gamma_c > 1)$. As illustrated for the standard run in Fig. 2 (magenta curve) and in Fig. 4 (top panel; magenta curve), $\gamma_c > 1$ and $\hat{x}_1(y_2) = 12.8°$.

3.2.2.2. Region B_2. Provided the wind is sufficiently strong, there is also a region in the basin filled by Rossby waves that emerge from the western boundary (Region B_2). The Region-A and Region-B_1 solutions are not valid there because they are determined by applying the eastern-boundary condition, $h_1(x_e) = h_e$. To obtain the Region-B_2 solution, h_w^+ must be specified in the latitude band where Rossby waves propagate away from the western boundary. Let $\bar{h}_w^+$ designate the values of h_w^+ in that band.

Because we do not resolve the structure of the western-boundary layer, it is not possible to determine $\tilde{h}_w^+$ from dynamical principles alone, and so we set $\tilde{h}_w^+ = h_{\min}$. This choice is sensible for several reasons. First, since $c_r^x(x_w^+)$ must be eastward in the band, the terms in square brackets in (22b) must be positive at the western boundary, which, for the parameters and forcings in the standard run, requires that $\tilde{h}_1^+ < 134 \, \mathrm{m} \approx h_{\min}$. Second, even if $\tilde{h}_1^+ \gtrsim h_{\min}$, Ekman pumping will rapidly ensure that h_1 thins to $h_{\min}$ in the interior ocean. Finally, a region corresponding to Region B$_2$ is present in the OGCM solutions and it has $\tilde{h}_w^+ \approx h_{\min}$ (Fig. 10).

With this choice for $\tilde{h}_w^+$, (22a) implies that $h_1 = h_{\min}$ throughout Region B$_2$: Rossby waves carry $\tilde{h}_w^+ = h_{\min}$ eastward and northward (assuming that Region B$_2$ lies within the Subpolar Gyre) and h_1 is maintained at $h_{\min}$ by the forcing terms. When Region B$_2$ extends south of Region B$_1$ (as is the case for a tiny part of Region B$_2$ in our standard run), part of the southern boundary of Region B is determined by Region B$_2$. In this case, characteristics emerging from the western boundary intersect those from the eastern boundary, and their intersection defines the boundary curve $\hat{x}_2(y)$ between Regions A and B$_2$. Furthermore, because the western- and eastern-boundary characteristics are associated with different values of h_1, h_1 jumps across $\hat{x}_2(y)$ to form a sharp front (shock).

We use the steady-state version of (22) to derive an equation for $\hat{x}_2(y)$. (See Dewar, 1991; Dewar et al., 2005, for discussions of similar "shock" solutions.) Since $|\nabla h_1| \to \infty$ across the front, and all other variables are continuous in (22a), the highest-order balance along $\hat{x}_2(y)$ is $\mathbf{c_r} \cdot \nabla h_1 = 0$, which can be rewritten

$$-\frac{\tau_{yy}^x}{D\beta}(x_e - x)h_{1x} - \frac{\beta g'}{f^2}\left(h_1^2\right)_x + \frac{\beta g'}{3Df^2}\left(h_1^3\right)_x + \frac{g_y'}{6Df}\left(h_1^3\right)_x + \left(\frac{f}{D\beta}w_{ek}\right)h_{1y} = 0.$$ (36)

We integrate (36) over the area of a box with the corners $[\hat{x}_2(y), y]$, $[\hat{x}_2(y), y + \Delta y]$, $[\hat{x}_2(y + \Delta y), y + \Delta y]$, and $[\hat{x}_2(y + \Delta y), y]$, which extends on either side of the front. In the limit that Δy is small, the coefficients of the h_1 terms are constant over the box, and the integral gives

$$\hat{x}_{2y} = \lim_{\Delta y \to 0}\frac{\Delta \hat{x}_2}{\Delta y} = \left[-\frac{\tau_{yy}^x}{D\beta}(x_e - x) - \frac{\beta g'}{2f^2}(h_A + h_{\min}) + \left(\frac{\beta g'}{3Df^2} + \frac{g_y'}{6Df}\right)\right.$$
$$\left.\left(h_A^2 + h_A h_{\min} + h_{\min}^2\right)\right]\left(\frac{f}{D\beta}w_{ek}\right)^{-1},$$ (37)

where $\Delta \hat{x}_2 \equiv \hat{x}_2(y + \Delta y) - \hat{x}_2(y)$ and $h_A \equiv h_1[\hat{x}_2(y), y]$ is the value of h_1 on the eastern flank of the front. Eq. (37) can be integrated from the southwestern edge of Region B$_2$, $(x_w^+, \hat{y}_s)$, to obtain $\hat{x}_2(y)$. Note that the right-hand side of (37) goes to c_r^x/c_r^y as $h_A \to h_{\min}$; therefore, (37) also defines $\hat{x}_2(y)$ when Region B$_2$ lies within Region B$_1$.

To illustrate the above ideas, Fig. 2 plots the curve $x_0(y)$ where $c_r^x = 0$, obtained by setting the term in square brackets in (22b) to zero and backsolving for $x = x_0(y)$ (orange curve). West of $x_0(y)$, $\}c_r^x > 0$ and hence the slope of characteristics is positive (white and red curves in Fig. 2). The latitude band where Rossby waves emerge from the western boundary lies between the two intersections of $x_0(y)$ with the western boundary. The thick red curve extending from the point $(x_w^+, \hat{y}_s = 36.6°\mathrm{N})$ indicates $\hat{x}_2(y)$ in Fig. 2; a shock exists only very near the western boundary, where the red curve extends south of the magenta one.

3.2.2.3. Currents. Since $h_1 = h_{\min}$ throughout Region B, the layer-1 flow there is given by the inviscid versions of (8a) with $h_1 = h_{\min}$,

$$U_1 = -\frac{D - h_{\min}}{D}\frac{g_y'}{2f}h_{\min}^2 - \frac{h_{\min}}{D}\frac{\tau_{yy}^x}{\beta}(x_e - x), \qquad x < \hat{x},$$ (38a)

$$V_1 = -\frac{\tau^x}{f} + \frac{h_{\min}}{D}\frac{f}{\beta}w_{ek}, \qquad x < \hat{x}.$$ (38b)

The layer-2 flow is non-zero, so that the total transport still adds up to the Sverdrup transport (12). The layer-2 circulation in Region B is apparent in Fig. 3 (arrows). The layer-1 flow, however, is too weak to be visible: It is dominated by weak southward Ekman drift, and the other contributions to (38) are small due to the factor $h_{\min}/D$.

For completeness, we note that if part of the southern boundary of Region B is determined by Region B$_2$ rather than B$_1$ (i.e., $\hat{x}_2 > \hat{x}_1$), a northeastward boundary current exists along $\hat{x}_2(y)$ there (A similar boundary current is also described by Parsons, 1969). It exists because of the shock in layer thickness, in which $h_1 = h_{\min}$ north of $\hat{x}_2(y)$ and is given by (25) south of it. Assuming that the along-boundary current is geostrophic, its transport is given by

$$\mathcal{V}_B = \frac{g'}{2f}\left[h_A^2 - h_{\min}^2 - \frac{2}{3D}\left(h_A^3 - h_{\min}^3\right)\right].$$ (39)

Eq. (39) is derived by integrating (8a) across the jump in h_1, e.g., from $\hat{x}_2 - \Delta x$ to $\hat{x}_2 + \Delta x$ and then taking the limit $\Delta x \to 0$. In the standard run, this current only exists very near the western boundary, where the red curve in Fig. 2 extends south of the magenta one.

There is upwelling throughout Region B. Substitution of (38) into the continuity equation gives the entrainment velocity

$$w_1 = w_e = -\frac{D - h_{\min}}{D}\left(\frac{\tau^x}{f}\right)_y = \frac{D - h_{\min}}{D}w_{ek},$$ (40)

which is essentially Ekman suction since $h_{\min} \ll D$. When $\gamma_c > 1$, as in the standard run, there is also entrainment in Region B$_1$ across the sidewall of layer 1 at $y = y_2$. Specifically, as layer-2 water moves southward across y_2, it entrains into the newly formed layer 1 at the rate,

$$w_c(y_2) = -V_1(y_2) = \frac{\tau^x}{f} - \frac{h_{\min}}{D}\frac{f^2}{\beta}w_{ek}, \qquad x < \hat{x}(y_2).$$ (41)

It is slightly less than the southward Ekman transport, as it is partly compensated by the northward, geostrophic gyre transport contained in the upper layer.

As reviewed in Section 1, entrainment similar to (40) also occurs in the solutions of Nonaka et al. (2006). It does not occur in the Huang (1986) and Huang and Flierl (1987) solutions because they do not allow for an exchange of mass between the layers; as a result, the upper layer entirely vanishes in Region B, thereby requiring a boundary current to conserve mass. Entrainment corresponding to (41) does not occur in any of the aforementioned studies models, because they do not have a northern region where the layer structure consists of a single layer.

3.3. Western boundary

The western-boundary solution is obtained by integrating Eqs. (16)-(18), starting in the north at y_2, and proceeding southward in the direction of Kelvin-wave propagation. First, the solution in the subpolar ocean ($\bar{y}_w \leqslant y \leqslant y_2$) is obtained numerically on a latitudinal grid, $Y_i = y_2 - (i - 1)\Delta y$, $i = 1, 2, 3, \ldots$, with $Y_1 = y_2$.

Evaluating (16) at Y_i and Y_{i-1}, subtracting the two expressions, and writing integrals in finite-difference form gives

$$\mathcal{V}_{1w}(Y_i) = \mathcal{V}_{1w}(Y_{i-1}) - W_w\left(Y_{i-\frac{1}{2}}\right)\Delta y + U_{1w}^+\left(Y_{i-\frac{1}{2}}\right)\Delta y, \qquad i \geqslant 2,$$ (42)

where $Y_{i-\frac{1}{2}} = Y_i - \Delta y/2$. Flow U_{1w}^+ is given either by U in (12) in Region A or by (38a) in Region B, both evaluated at $x = x_w^+$. The solution to (42) requires that $\mathcal{V}_{1w}(Y_1) = \mathcal{V}_{1w}(y_2)$ is known, and it is given in (17a).

It remains to evaluate $W_w(Y_{i-\frac{1}{2}})$ at each point in the integration. In a first step, we set $W_w = 0$ in (42) to calculate a preliminary boundary-current transport, $\mathcal{V}'_{1w}(Y_i)$. In a second step, we set $h_w = -$

h_{min} in Eqs. (18) to calculate a second test-transport, $\tilde{V}_{1w}(Y_i)$. Because V_{1w} increases as h_w decreases (see Eq. (18)) and entrainment ensures that $h_w \geqslant h_{min}$, it follows that $\tilde{V}_{1w}(Y_i)$ is the upper limit for the boundary-current transport (i.e., $V_{1w} \leqslant \tilde{V}_{1w}$). Therefore, if $V'_{1w} > \tilde{V}_{1w}$, (42) cannot be satisfied with $W_w\left(Y_{i-\frac{1}{2}}\right) = 0$, and so we set $h_w = h_{min}, V_{1w}(Y_i) = \tilde{V}_{1w}(Y_i)$, and calculate $W_w\left(Y_{i-\frac{1}{2}}\right)$ from (42). Conversely, if $V'_{1w} \leqslant \tilde{V}_{1w}$, we set $V_{1w}(Y_i) = V'_{1w}(Y_i)$, $W_w\left(Y_{i-\frac{1}{2}}\right) = 0$, and, if desired, solve (18) for h_w.

With $V_{1w}(\bar{y}_w)$ known, and since there is by assumption no western-boundary upwelling in the subtropics ($W_w = 0$ at $y < \bar{y}_w$), transports at $y < \bar{y}_w$ are obtained directly by integrating the layer-1 continuity equation from x_w to x_w^+ and from y to $\bar{y}_w$,

$$
\begin{aligned}
V_{1w}(y) &= V_{1w}(\bar{y}_w) - \int_y^{\bar{y}_w} U_{1w}^+ dy \\
&= V_{1w}(\bar{y}_w) - \frac{1}{\beta}\tau_x^x(x_e - x_w), \qquad y < \bar{y}_w.
\end{aligned}
\tag{43a}
$$

In deriving (43a), we use the properties that the interior flow field is in Sverdrup balance and contained entirely in layer 1 so that $U_{1w}^+ = -\Psi_y$ (see the discussion after Eq. (23)) and the property that $\Psi(x, \bar{y}_w) = 0$. A similar integral of the layer-2 continuity equation gives

$$
V_{2w}(y) = V_{2w}(\bar{y}_w) = -V_{1w}(\bar{y}_w), \qquad y < \bar{y}_w,
\tag{43b}
$$

the latter statement following from the fact that $V_{1w}(\bar{y}_w) + V_{2w}(\bar{y}_w) = V(\bar{y}_w) = 0$ by (15). According to (43), layer 1 contains all of the wind-driven, western-boundary current as well as the constant MOC upper branch $V_{1w}(\bar{y}_w)$, and layer 2 contains the MOC lower branch that balances $V_{1w}(\bar{y}_w)$.

Fig. 5 plots the resulting profiles of V_{1w}, V_w from (15), and $V_{2w} = V_w - V_{1w}$ for the standard run; it also plots the cumulative western-boundary entrainment from the northern boundary, $W_w = \int_y^{y_2} W_w dy$, with $W_w(y_2) = -V_{1w}(y_2)$ being the entrainment across the sidewall of layer 1 due to w_c. As discussed next, properties of the western-boundary transports change in the intervals, $\hat{y}_s < y \leqslant y_2$, $\bar{y}_w < y < \hat{y}_s$, and $y < \bar{y}_w$.

Since Region B extends from $\hat{y}_s$ to y_2 in the standard run, $h_w^+ = h_{min}$ and U_{1w}^+ is given by (38a) in that interval. It is then
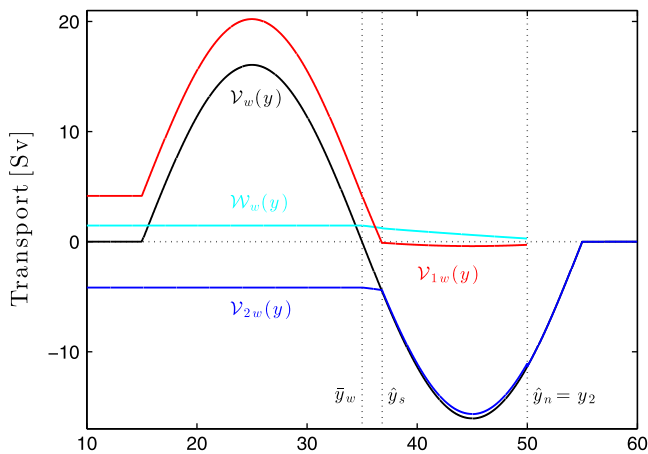

Fig. 5. Meridional profiles of western-boundary-current transports in layer 1 V_{1w} (red curve) and layer 2 V_{2w} (blue curve) in the VLOM standard solution with $H_s = 250$ m and $\tau_o = 0.12$ Nm^{-2} (The interior solution is shown in Fig. 3). Also shown are the barotropic boundary-current transport V_w (black curve), and the western-boundary entrainment integrated southward from y_2, W_w (cyan curve). The unit is Sv. The dotted lines indicate the latitudes $\bar{y}_w$, $\hat{y}_s$ and $\hat{y}_n$. (For interpretation of the references to colour in this figure legend, the reader is referred to the web version of this article.)

straightforward to show that $V'_{1w} \geqslant \tilde{V}_{1w}$ throughout the interval. Consequently, $h_w = h_{min}$,

$$
V_{1w} = \tilde{V}_{1w} = -\frac{h_{min}}{D}\frac{\tau_y^x}{\beta}(x_e - x_w), \qquad \hat{y}_s \leqslant y \leqslant y_2,
\tag{44a}
$$

and

$$
W_w = \tilde{V}_{1wy} + U_{1w}^+ = -\frac{D - h_{min}}{D}\frac{g'_y}{2f}h_{min}^2, \qquad \hat{y}_s \leqslant y < y_2.
\tag{44b}
$$

Because $h_w = h_w^+$, the meridional current does not have a baroclinic structure (i.e., depth-averaged meridional velocities are the same in layers 1 and 2); thus, the layer-2 transport is much larger than the layer-1 transport because $h_1 \ll h_2$ (compare red, blue, and black curves north of $\hat{y}_s$). Entrainment W_w increases to the south since $W_w \neq 0$ (cyan curve in Fig. 5).

In the interval from $\bar{y}_w$ to $\hat{y}_s$, h_w^+ is given by (25) and is deeper than h_{min}. Consequently, the baroclinic term in square brackets in (18) is positive. It is strong enough to reverse the weak southward flow from the last term, so that $V_{1w} > 0$ (red curve in Fig. 5). This northward transport provides an additional source (other than W_w) to feed the eastward interior flow given by (12). In the standard solution, however, it is still too weak to eliminate the need for upwelling (i.e., $\mathcal{D}$ is large in Eq. (17b)), and so $h_w = h_{min}$ throughout the Subpolar Gyre. In addition, the upwelling in the interval is even stronger than it is farther to the north (the slope of the cyan curve is steeper than farther north), because the offshore, upper-layer transport, U_{1w}^+, is larger in $\mathcal{D}$.

South of $\bar{y}_w$, transports are determined by (43). Accordingly, W_w and V_{2w} remain constant, and V_{1w} has a recirculation part of the Subtropical Gyre on top of the constant MOC part.

3.4. Shear flow

The total velocity field within layer 1 is given by (19), and consists of depth-averaged and shear parts. Just offshore from the eastern boundary, $h_1 = h_e(y)$, ensuring that the depth-averaged component of u_1 vanishes. The shear flow of u_1 remains, however, consisting of eastward (westward) flow in the upper (lower) part of layer 1 in the region where $T_y^* \neq 0$ (upper-left panel of Fig. 6). Right at the eastern boundary, that circulation is closed in a horizontal Ekman layer, where water sinks (upper-right panel of Fig. 6; see Schloesser et al., 2012). The maximum sinking transport/width at the eastern boundary occurs at a depth of $z' = -h_e/2$, which by continuity is

$$
W_e(y) \equiv \int_{x_e^-}^{x_e} w(x, y, z') \, dx = -\int_{-h_e/2}^0 u_1(x_e^-, y, z) \, dz = \frac{g'_y}{8f}h_e^2,
\tag{45}
$$

where $x_e^- = x_e - \Delta x$ is a longitude just west of the eastern-boundary layer. Downwelling (45) corresponds to the eastern-boundary sinking found in the OGCM solutions of Spall and Pickart (2001); however, in our model it occurs isothermally and is not related to diapycnal overturning.

In the interior ocean, a consequence of the thermal-wind shear is that layer-1 currents are surface (bottom) intensified in regions of eastward (westward) Sverdrup flow (bottom-left panel of Fig. 6). South of 30°N, there is no shear flow since $g'_y = 0$. From 30 to 42°N, the depth-averaged flow is eastward, the shear flow has about the same strength, and hence the eastward flow is surface intensified. North of 47°N, where h_1 is thick, the depth-averaged flow is weak but the shear flow is large; as a result, velocities are eastward in the upper part of the layer, even though the Sverdrup transport is westward. From 42 to 47°N, the section intersects Region B, so that $h_1 = h_{min}$ and both zonal-velocity components are small: the Sverdrup part because it is distributed over the entire water column, and the shear part because the upper layer is thin.
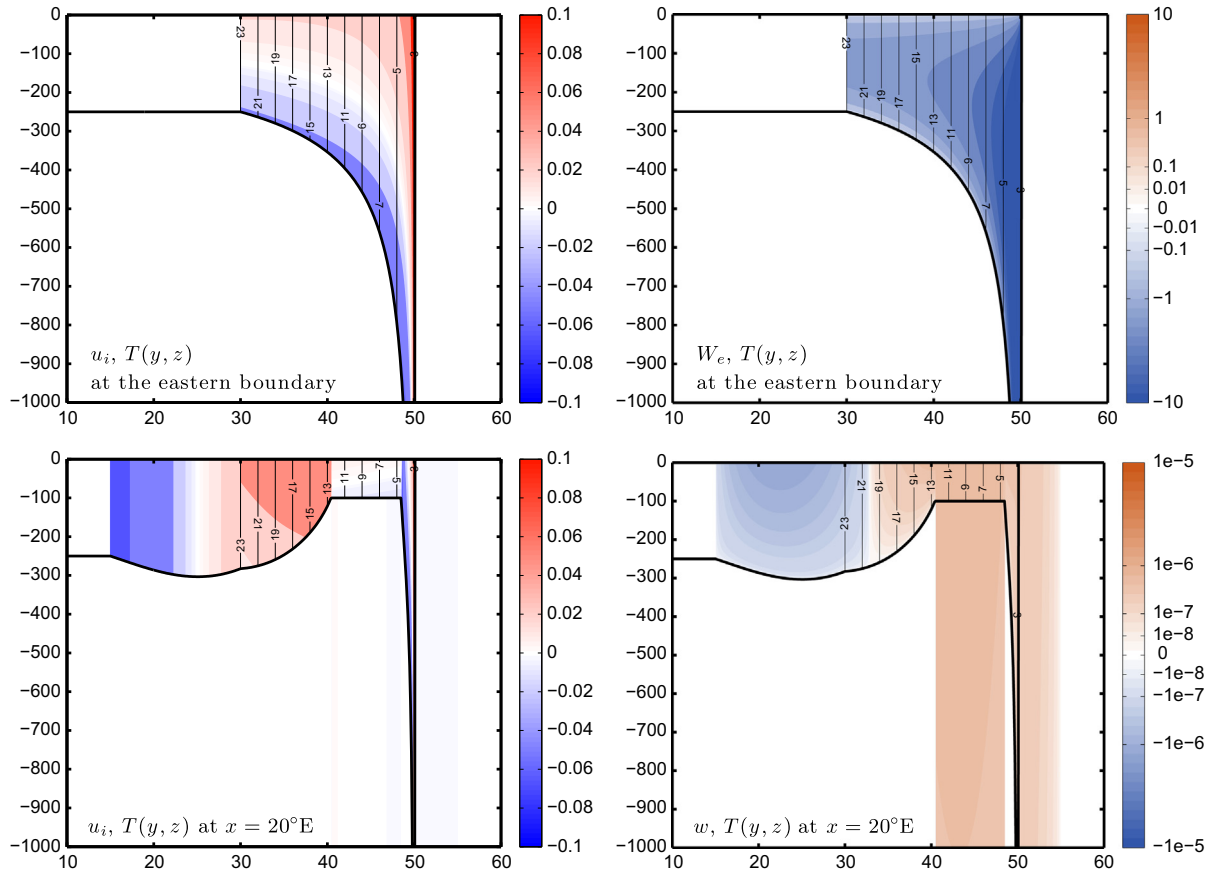
Fig. 6. Meridional sections of depth-dependent, zonal velocities (shading, left panels) and vertical transports/velocities (shading, right panels) at the eastern boundary (upper panels), and at $x = 20°E$ (lower panels), for the VLOM standard solution with $H_s = 250$ m, $\tau_o = 0.12$ N/m², $h_{\min} = 100$ m, $D = 4000$ m and $w_d = 0$. The thick, black curve indicates the layer interface, and thin contours correspond to isotherms.

Vertical motion w in the interior ocean is given by (19b) and (19d). In Region A, w is confined to layer 1 since $w_1 = 0$, and its direction is determined by the sign of the Ekman pumping w_{ek} (bottom-right panel of Fig. 6). In Region B (42°N $\lesssim y \lesssim$ 47°N in Fig. 6) and to the north of y_2 (>50°N), w and w_{ek} extend to the ocean bottom. Note that interior sinking is confined to the upper ocean in the Subtropical Gyre; deep sinking of cold water occurs only near the eastern boundary, where it is given by (45).

4. Solution with $w_d \neq 0$

The standard run illustrates how northward flow in the Subpolar Gyre can generate the surface convergence needed to establish the MOC descending branch. In OGCMs, however, mixing tends to restratify the water column in the northern ocean, providing another process for generating MOC downwelling (Schloesser et al., 2012). Here, we extend the solution obtained in Section 3 to include that process by allowing $w_d \neq 0$. In this case, solutions have a northern-boundary layer (Region N) just south of y_2 where $h_e(y) > h_{\max}$, and w_d relaxes h_1 back to $h_{\max}$ there. Because $h_1 < h_{\max}$ everywhere outside Region N, the solution of Section 3 is *unchanged* in Regions A and B. In the following, then, we obtain the solution in Region N and determine its influence on the western-boundary currents.

The analytic solution obtained here requires that $t_d \to 0$ in w_d. As a result, all detrainment is confined to an eastern-boundary layer, and $w_1 = w_d = 0$ in the interior of Region N. When t_d is finite, the eastern-boundary layer broadens into the interior of Region N, the two regions are no longer dynamically distinct, and the solution must be obtained by numerical integration. For our purposes, the $t_d \to 0$ restriction is reasonable because we are interested in understanding the impact of w_d on the large-scale MOC, which does not change appreciably provided that t_d is short compared to the time it takes Rossby waves to cross the basin.

4.1. Definitions

Region N lies north of the characteristic curve, $y''(x)$, that extends from the point (x_e, y''_e), where y''_e is the latitude at which h_e first deepens to $h_{\max}$. Since $y''(x)$ lies on the edge of Region A, (28) holds so that $y''(x)$ is the inverse function of $x_Y(y, Y)$ with $Y = y''_e$. The upper-middle panels in Fig. 4 show the $w_d \neq 0$ solution that uses the standard-run parameters and forcing and with $h_{\max} = 750$ m in a meridionally expanded view. With these parameter choices, characteristic $y''(x)$ (gray curve) satisfies (29) and so extends from (x_e, y''_e) to the focal point $[\hat{x}(y_2), y_2]$. For smaller values of τ_o or larger values of H_s (so that $\gamma_c < 1$), the characteristic intersects the western boundary at $y''(x_w) \equiv y''_w$ (lower-middle panels of Fig. 4), and when $\tau_o = 0$ the southern boundary is flat, that is, $y''(x) = y''_e$ (bottom panels of Fig. 4); in these cases, Region N has a western edge just outside the western-boundary layer at $x = x_w^+$. [3]

4.2. Eastern-boundary layer

The inclusion of w_d generates an eastern-boundary layer in Region N. Because $t_d \to 0$ in (10b), w_d causes h_1 to jump from h_e at $x = x_e$ to $h_{\max}$ just offshore at $x = x_e^-$. As a result, there is a geo-

strophic current along the eastern boundary with the upper-layer transport

$$\mathcal{V}_{1e}(y) \equiv \int_{x_e^-}^{x_e} \frac{\langle p_{1x} \rangle}{f} dx = \frac{g'}{Df}\left[\frac{D}{2}(h_e^2 - h_{max}^2) - \frac{1}{3}(h_e^3 - h_{max}^3)\right], \quad (46a)$$

where contributions from the τ^x and ψ integrals vanish in the limit that $x_e^- \to x_e$. Note that $\mathcal{V}_{1e}(y_e'') = \mathcal{V}_{1e}(y_2) = 0$ since $h_e(y_e'') = h_{max}$ and $g'(y_2) = 0$, so that there is no flow across the meridional boundaries of Region N. There is also a zonal transport into the coast given by

$$U_1(x_e^-, y) = -U_2(x_e^-, y) = -\frac{D - h_{max}}{2Df} g' h_{max}^2. \quad (46b)$$

This convergence and the corresponding eastern-boundary detrainment by w_d are evident in all solutions with $w_d \neq 0$ in Fig. 4. Because Eqs. (46) do not depend on the wind forcing, the eastern-boundary circulation is identical in all three cases shown; it is also the same in the solutions of Schloesser et al. (2012).

4.3. Interior-ocean response

As in Region A, the response in the interior of Region N is described by (22a) with $w_1 = 0$. Because $U_2(x_e^-, y) \neq 0$, however, the property that $\mathbf{v}_2 = 0$ no longer holds and so (24) is not valid. To obtain a solution, we rewrite (23) as $q(x, y) = \mathcal{Q}(\psi_2)$. It follows that $\nabla q(x, y) = \mathcal{Q}_{\psi_2} \nabla \psi_2$ and, since $\mathcal{Q}$ depends only on ψ_2 (not explicitly on x or y), along layer-2 streamlines $\mathcal{Q}_{\psi_2} = a$ where a is a constant. As noted just below (23), when $w_1 = 0$ characteristic curves are parallel to isolines of q and hence to layer-2 streamlines. Therefore, along any characteristic curve in Region N, both $\psi_{2x}/q_x = V_2/q_x = a$ and $\psi_{2y}/q_y = -U_2/q_y = a$ hold, and we can write

$$\frac{V_2[x_r(y), y]}{q_x[x_r(y), y]} = -\frac{U_2[x_e^-, y_r(x_e^-)]}{q_y[x_e^-, y_r(x_e^-)]}, \quad (47)$$

where the characteristic is designated by $y_r(x)$ or its inverse $x_r(y)$.

To obtain an expression that can be zonally integrated along a latitude circle, we rewrite the right-hand side of (47) in terms of variables evaluated at y rather than $y_r(x_e^-)$. Since $U_2[x_e^-, y_r(x_e^-)]$ is given by (46b), and definition (27) implies that

$$q_y[x_e^-, y_r(x_e^-)] = -\frac{\beta[y_r(x_e^-)]}{f^2[y_r(x_e^-)]}(D - h_{max}), \quad (48)$$

the only latitude-dependent variables that need to be replaced in (47) are f and β. Using (27), and the property that q is constant along characteristics, we have

$$f[y_r(x_e^-)] = \frac{f(y)(D - h_{max})}{h_2[x_r(y), y]}. \quad (49)$$

Variables f and β are related by the identity, $f^2 + (R_e\beta)^2 = 4\Omega^2$, where R_e is the radius of the earth and $\Omega = 2\pi$ day^{-1}. With the aid of (49), that identity can be rewritten

$$\beta[y_r(x_e^-)] = \frac{f(D - h_{max})}{R_e h_2}\sqrt{\alpha^2 h_2^2 - 1},$$

$$\alpha^{-1} \equiv (D - h_{max})\sin\left(\frac{y}{R_e}\right), \quad (50)$$

where h_2, f, and α are evaluated at $[x_r(y), y]$. Setting $V_2 = \langle p_{2x} \rangle/f$, $q_x = -h_{2x}/f$, and using (46b), (48), (49) and (50), and the approximation $h_{1x} \approx -h_{2x}$ (which is consistent with the level of approximation in our baroclinic equations), (47) can be rewritten

$$\frac{g'(D - h_2)h_2}{D} + \frac{h_2}{D}\frac{f^2}{\beta}\frac{w_{ek}}{h_{2x}} = \frac{g'_y h_{max}^2}{2D}\frac{R_e}{\sqrt{\alpha^2 h_2^2 - 1}}, \quad (51)$$

with both sides of (51) now evaluated at the point $[x_r(y), y]$. Since $x_r(y)$ corresponds to any characteristic curve that intersects y within Region N, (51) holds for *all* x and y therein, and we can set $x_r(y) = x$.

After some reorganization, we zonally integrate (51) using the boundary condition $h_2(x_e^-) = D - h_{max}$, the identity $\left(h_2\sqrt{\alpha^2 h_2^2 - 1}\right)^{-1} h_{2x} = -[\sin^{-1}(\alpha h_2)^{-1}]_x$, and the definition of α rewritten as $y/R_e = \sin^{-1}[\alpha^{-1}(D - h_{max})^{-1}]$. With the replacement $h_1 = D - h_2$, the result is

$$h_1 = D - \frac{(D - h_{max})\sin\frac{y}{R_e}}{\sin\left[\frac{y}{R_e} + \frac{2(f^2/\beta)w_{ek}(x_e^- - x)}{g'_y R_e h_{max}^2} - \frac{g'}{g'_y R_e}\frac{h_{max}^2 - h_1^2}{h_{max}^2}\right]}, \quad (52)$$

an implicit equation for $h_1(x, y)$ that can be readily solved numerically. Note that because $\sin(y/R_e) = f(y)/(2\Omega)$, (52) is essentially a statement of PV-conservation along characteristics in layer 2, analogous to (27) in Region A, with the argument of the denominator in (52) giving the latitude where the characteristic intersects with $x = x_e^-$. Furthermore, when evaluated along $y = y_2$ (52) simplifies to

$$h_1 = D - \frac{(D - h_{max})\sin\frac{y}{R_e}}{\sin\left[\frac{y}{R_e} + \frac{2(f^2/\beta)w_{ek}(x_e^- - x)}{g'_y R_e h_{max}^2}\right]}, \quad y = y_2, \quad (53)$$

since $g'(y_2) = 0$, an *explicit* expression for $h_1(x, y_2)$ since the right-hand side no longer involves h_1. With h_1 known everywhere in Region N, so are the transports.

A noteworthy feature of the solutions in Fig. 4 is that h_1 does not vary much throughout Region N (the interval between white contours in the left-middle panels is only 10m). The small meridional change is understandable since Region N is so narrow. The small zonal variation is particularly interesting (counterintuitive), given that in a $1\frac{1}{2}$-layer model the zonal slope would be much larger (the same as in Region A). It happens because of (47), the constraint that PV is conserved in layer 2; this constraint is not considered in a $1\frac{1}{2}$-layer model, which neglects layer-2 flow altogether.

4.4. Western boundary

In solutions where Region N has no western edge ($\gamma_c > 1$), U_{1w}^+ is unchanged from the standard run, and so allowing $w_d \neq 0$ does not affect the western-boundary response at all. If Region N has a western edge ($\gamma_c < 1$), the transport/width across x_w^+ is

$$U_{1w}^+ = -\frac{D - h_w^+}{D}\frac{\left(g'h_w^{+2}\right)_y}{2f} - \frac{h_w^+}{D}\frac{\tau_{yy}^x}{\beta}(x_e - x_w^+), y_w'' \leqslant y \leqslant y_2, \quad (54)$$

where h_w^+ is given by (52) with $x = x_w^+$. The western-boundary solution is then obtained using the same procedure as in Section 3.3. Note that because the western-boundary response is obtained by integrating southward from $y = y_2$, the western-boundary current is impacted *everywhere* along the boundary, even though U_{1w}^+ differs from the standard run only north of y_w''. As discussed in Section 5, the impact on the western-boundary transport can be significant.

5. Overturning transports

We define the transport $\mathcal{M}$ of the large-scale MOC to be the aggregate of all across-interface transports in the subpolar ocean,

$$\mathcal{M} \equiv \mathcal{M}_n - \mathcal{M}_{in} - \mathcal{W}_w = -\left(\mathcal{W}_d + \mathcal{W}_c^-\right) - \left(\mathcal{W}_b + \mathcal{W}_c^+\right) - \mathcal{W}_w. \quad (55)$$

Transport $\mathcal{W}_d$ is the detrainment in Region N due to $w_d, \mathcal{W}_b = \int_B w_e dA$ is the area integral of (40) over Region B, and $\mathcal{W}_w = \int_{y_w}^{y_2} W_w dy$ is the entrainment in the western-boundary layer determined as described in Section 3.3. Transports

$\mathcal{W}_c^{\pm} = \int_{x_w^+}^{x_e} w_c \, \theta(\pm w_c) dx$ are the interior entrainment and detrainment transports across the sidewall of layer 1 at $y = y_2$, which occur west and east of $\hat{x}(y_2)$, respectively.

The total detrainment $\mathcal{M}_n = -(\mathcal{W}_d + \mathcal{W}_c^-)$ and entrainment $\mathcal{M}_{in} = \mathcal{W}_b + \mathcal{W}_c^+$ terms are of interest in themselves. Transport $\mathcal{M}_n$ is the net formation of deep water in the northern ocean. Transport $\mathcal{M}_{in}$ is the net entrainment of deep water into layer 1 in the interior of the northern ocean. Together, $\mathcal{M}_{in}$ and $\mathcal{W}_w$ provide an overturning "shortcut" for the MOC, so that $\mathcal{M}$ is less than $\mathcal{M}_n$.

5.1. Detrainment $\mathcal{M}_n$

5.1.1. $w_d = 0$ case

When $w_d = 0$, w_c is given by (30) and

$$\mathcal{M}_n = -\mathcal{W}_c^- = -\int_{\hat{x}}^{x_e} w_c \, dx = -\frac{\tau_y^x}{\beta}(x_e - \hat{x}), \quad y = y_2, \quad (56)$$

that is, it is the Sverdrup transport across y_2 east of $\hat{x}(y_2)$. When $\gamma_c \leqslant 1$, we define $\hat{x}(y_2) = x_w^+$ for notational convenience and the integral extends over the entire basin so that

$$\mathcal{M}_n = -\frac{\tau_y^x}{\beta}(x_e - x_w^+), \quad y = y_2, \quad \gamma_c \leqslant 1. \quad (57a)$$

When $\gamma_c > 1$, (26) with $y = y_2$ can be used to eliminate $(x_e - \hat{x})$ to get

$$\mathcal{M}_n = \frac{g_s'}{2f} H_s^2 C_\tau, \quad \text{with} \quad C_\tau \equiv \frac{-\tau_y^x/\beta}{\tau^x/f - \tau_y^x/\beta}, \quad y = y_2, \quad \gamma_c > 1. \quad (57b)$$

Therefore, $\mathcal{M}_n$ is proportional to the wind amplitude τ_o when $\gamma_c \leqslant 1$, but is *independent* of it when $\gamma_c > 1$ because wind terms appear in both the numerator and denominator of C_τ in (57b). Expressed in physical terms, the independence happens when $\gamma_c > 1$, because an intensification of the Sverdrup transport across y_2 due to an increase in τ_o is exactly compensated by a decrease in the length, $x_e - \hat{x}(y_2)$, over which it occurs.

Fig. 7 plots $\mathcal{M}_n$ as function of τ_o for the standard run ($w_d = 0$, blue curve). Its form changes markedly at a critical wind amplitude, $\tau_c = 0.082$ N/m^2, the value of τ_o where $\gamma_c = 1$. Consistent with Eqs. (57), $\mathcal{M}_n$ increases linearly with τ_o for $\tau_o < \tau_c$, whereas it is constant for $\tau_o > \tau_c$.

Fig. 8 (top panel) illustrates the dependence of $\mathcal{M}_n$ on both H_s and τ_o when $w_d = 0$, plotting $\mathcal{M}_n(H_s)$ in solutions for four values of τ_o. From its definition in (35), it follows that $\gamma_c > 1$ when $H_s < H_c$. In that range, then, $\mathcal{M}_n(H_s)$ satisfies (57b), and so is independent of τ_o and grows parabolically with H_s. When $H_s \geqslant H_c$, $\mathcal{M}_n(H_s)$ satisfies (57a), and remains constant for $H_s \geqslant H_c$ (dashed curves). (The property holds for the $\tau_o = 0$ solution as well, except that $\mathcal{M}_n = 0$ is the maximum value in that case.) The maximum value of $\mathcal{M}_n$ and critical layer thickness H_c vary among the solutions, both increasing with τ_o.

Remarkably, (57b) exhibits the same relation between meridional pressure difference $\left(g_s' H_s^2/2\right)$ as derived from scaling arguments and in solutions without winds (Park and Bryan, 2000; Schloesser et al., 2012, Eqs. (1) and (2) in this manuscript). The difference is that C_τ depends on the wind forcing rather than the coefficient of diffusive mixing, a statement that flow within the Subpolar Gyre provides another mechanism (other than Rossby-wave damping) for causing the MOC surface branch to converge into the northern ocean. Since $\tau^x > 0$, $\tau_y^x < 0$ and $\tau^x/f < -\tau_y^x/\beta$ in the Subpolar Gyre, it follows that C_τ satisfies the inequality, $\frac{1}{2} < C_\tau < 1$, its value being closest to one in the northern part of the gyre where the Ekman transport is small.
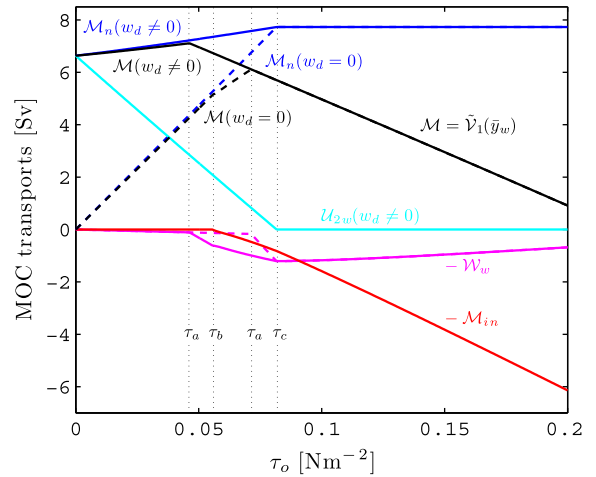

Fig. 7. Profiles of MOC transports as a function of τ_o for the VLOM standard run ($w_d = 0$) and the corresponding solution with $w_d \neq 0$, showing $\mathcal{M}$ (solid/dashed black line), $\mathcal{M}_n$ (solid/dashed blue curve), $\mathcal{U}_{2w}$ for the $w_d \neq 0$ solution (cyan curve), $\mathcal{M}_{in}$ (red curve) and $\mathcal{W}_w$ (solid/dashed magenta line). Curves for the $w_d \neq 0$ run are solid everywhere. Curves for the standard solution are the dashed, except in the regions where the transports are the same as in the $w_d \neq 0$ solution and curves are solid. The unit of all transports is SV. In the $w_d \neq 0$ solution, $H_s = 250$ m and $h_{max} = 750$ m. The critical wind strengths τ_a, τ_b and τ_c are indicated by vertical, dotted lines; the smaller one of the two τ_a corresponds to the solutions with $w_d \neq 0$. (For interpretation of the references to colour in this figure legend, the reader is referred to the web version of this article.)

5.1.2. $w_d \neq 0$ case

When $w_d \neq 0$, detrainment within Region N also contributes to $\mathcal{M}_n$. Since $h_1 < h_{max}$ west of x_e^-, *all* the w_d detrainment occurs at the eastern boundary. With the aid of (6) and (21), which give the relations $g_y' = -g'(y_e'')/(y_2 - y_e'')$ and $g'(y_e'')h_{max}^2 = g_s'H_s^2$, and (46b), continuity requires that its net contribution is

$$\mathcal{W}_d = \int_{x_e^-}^{x_e} \int_{y_e''}^{y_2} w_d \, dx \, dy = -\int_{y_e''}^{y_2} U_1(x_e^-, y) dy$$
$$= \frac{D - h_{max}}{2D} \overline{f^{-1}} g_s' H_s^2, \quad (58)$$

where $\overline{f^{-1}} = \int_{y_e''}^{y_2} f^{-1} dy/(y_2 - y_e'')$ is the average of f^{-1} over the latitudinal extent of Region N. Since the flow in the eastern-boundary layer is not affected by the wind forcing, detrainment (58) is the same as in Schloesser et al. (2012).

The layer-1 detrainment across y_2 in Region N is

$$\mathcal{W}_c^- = \int_{\hat{x}}^{x_e} w_c dx = -\int_{\hat{x}}^{x_e} V_1 dx = -\int_{\hat{x}}^{x_e} (V - V_2) dx$$
$$= \frac{\tau_y^x}{\beta}(x_e - \hat{x}) + \int_{\hat{x}}^{x_e} V_2 dx, \quad y = y_2, \quad (59)$$

and it does not simplify to (56) because $V_2(x, y_2) \neq 0$ when $w_d \neq 0$. To evaluate the V_2 integral, consider the wedge-shaped region bounded by $y = y_2$, $x = x_e^-$ and the characteristic $\tilde{x}_Y$ that intersects the northwestern corner of Region N, that is, the point $[\hat{x}(y_2), y_2]$ (see the lower-middle right panel of Fig. 4). Since characteristics are also layer-2 streamlines, an area integral of the layer-2 continuity equation gives

$$\int_{\hat{x}(y_2)}^{x_e} V_2(x, y_2) dx = -\int_Y^{y_2} U_2(x_e^-, y) dy = \int_Y^{y_2} U_1(x_e^-, y) dy, \quad (60)$$

with Y being the latitude where characteristic $\tilde{x}_Y$ intersects the eastern boundary. Next, we solve for Y, using (53) and (27) with $y = y_2$ and $h_1(x_e^-, Y) = h_{max}$, to get

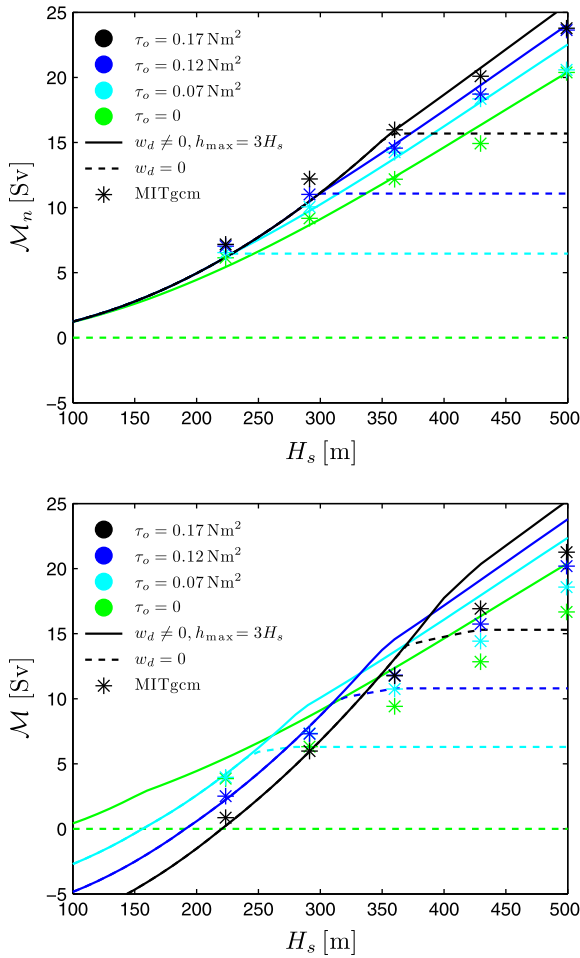$$Y = y_2 + 2\frac{f^2}{\beta}\frac{w_{ek}}{g_y' h_{max}^2}(x_e - \hat{x}), \quad y = y_2. \quad (61)$$

Fig. 8. Profiles of $\mathcal{M}_n$ (upper panel) and $\mathcal{M}$ (lower panel) as a function of H_s in VLOM solutions with $w_d = 0$ and $w_d \neq 0$ and for four different wind strengths: $\tau_o = 0$ (green), 0.07 N/m^2 (cyan), 0.12 N/m^2 (blue) and 0.17 N/m^2 (black). Curves for the $w_d \neq 0$ solutions are solid everywhere. Curves for the $w_d = 0$ solution are the solid, except in the regions where the curve is dashed. Also shown are MITgcm data points (stars), indicating max (ψ^T) in the upper and max[ψ^T ($\bar{y}_w$)] in the lower panel, and using the same color code as for the VLOM solutions. The unit of the transports is Sv. (For interpretation of the references to colour in this figure legend, the reader is referred to the web version of this article.)

Note that when $\hat{x}(y_2) > x_w^+(\gamma_c > 1)$, the corner characteristic $\tilde{x}_Y$ coincides with the streamline $y''(x)$, so that $Y = y_e''$ (upper-middle panel of Fig. 4). This property also follows directly from (61), using (28) evaluated at $y = y_2$ so that $\tilde{x}_Y(y_2) = \hat{x}(y_2)$, and the relations $g_y' = -g'(y_e'')/(y_2 - y_e'')$ and $g'(y_e'')h_{\max}^2 = g_s'H_s^2$.

Eqs. (59), (60), and (46b) combine to give

$$\mathcal{W}_c^- = \frac{\tau_y^x}{\beta}(x_e - \hat{x})\Big|^{y_2} - \frac{D - h_{\max}}{2D}g_y'h_{\max}^2 \int^{y_2}_Y f^{-1}dy. \tag{62}$$

According to (62), in comparison to the $w_d = 0$ solution, $\mathcal{W}_c^-$ is reduced by the amount of water that detrains along the eastern boundary north of Y; moreover, when $\gamma_c > 1$ and $Y = y_e''$, the amount equals $\mathcal{W}_d$ so that $\mathcal{W}_c^-$ is reduced by *all* the detrainment in Region N.

In either case, the *total* detrainment is

$$\mathcal{M}_n = -(\mathcal{W}_c^- + \mathcal{W}_d) = \frac{\tau_y^x}{\beta}(x_e - \hat{x})\Big|^{y_2} + \mathcal{U}_{2w}, \tag{63a}$$

where

$$\mathcal{U}_{2w} = \frac{D - h_{\max}}{2D}g_y'h_{\max}^2 \int^Y_{y_e''} f^{-1}dy. \tag{63b}$$

From the layer-2 continuity equation, $\mathcal{U}_{2w} = -\int^Y_{y_e''} U_2(x_e^-, y)dy = -\int^{y_2}_{y_w''} U_2(x_w^+, y)dy$, so that $\mathcal{U}_{2w}$ is the westward transport in layer 2 that crosses x_w^+ south of y_2 in the range $y_w'' \leqslant y \leqslant y_2$. When $\gamma_c < 1$ and $Y > y_e''$, $\mathcal{U}_{2w} > 0$ and hence increases $\mathcal{M}_n$ (lower-middle right panel in Fig. 4). When $\gamma_c \geqslant 1$ and $Y = y_e''$, however, Region N does not extend to the western-boundary layer, all the water that is detrained by w_d near the eastern boundary crosses y_2 before joining the deep western-boundary current, and hence $\mathcal{U}_{2w} = 0$ (upper-middle right panel in Fig. 4). In this case, $\mathcal{M}_n$ reduces to (57b), that is, it has the same value as in the $w_d = 0$ solution.

Fig. 7 plots $\mathcal{M}_n(\tau_o)$ when $w_d \neq 0$, $h_{\max} = 3H_s = 750$ m, and all other parameters as in the standard run (blue curve). The transport again increases linearly with wind strength until $\tau_o = \tau_c(\gamma_c = 1)$ and thereafter is the same as in the standard run. For $\tau_o < \tau_c$, $\mathcal{U}_{2w}$ (cyan line) also contributes to $\mathcal{M}_n$, so that $\mathcal{M}_n \neq 0$ when $\tau_o = 0$; as τ_o increases, $\mathcal{U}_{2w}$ decreases as the meridional extent of the western boundary of Region N ($y_2 - y_w''$) diminishes, and it vanishes when $\tau_o = \tau_c$.

Fig. 8 (top panel) plots $\mathcal{M}_n(H_s)$ when $w_d \neq 0$ and with $h_{\max} = 3H_s$ (solid curves everywhere). The curve deviates from the profile with $w_d = 0$ only for $H_s > H_c(\mathcal{U}_{2w} > 0)$, where $\mathcal{M}_n$ continues to grow due to the contribution from $\mathcal{U}_{2w}$.

5.2. Entrainment $\mathcal{M}_{in}$

Recall that w_d, which occurs only within Region N, does not affect the solution in Regions A and B at all. Thus, the following derivation of $\mathcal{M}_{in}$, which utilizes transports from Regions A and B assuming that $w_d = 0$, is also valid when $w_d \neq 0$.

When $\gamma_b > 1$, there is entrainment due to w_e in (40) wherever layer 2 outcrops ($h_1 = h_{\min}$). In addition, if $\gamma_c > 1$, so that the boundary of Region B intersects y_2 at $\hat{x}(y_2) > x_w^+$, there is also entrainment due to w_c in (41). For the first part, an area integral of the layer-1 continuity equation over Region B gives

$$\mathcal{W}_b = \int_B w_1 \, da = \int^{x_e}_{x_w^+} V_1(x, \hat{y}_n)dx - \int^{x_e}_{x_w^+} V_1(x, \hat{y}_s) \, dx - \int^{\hat{y}_n}_{\hat{y}_s} U_{1w}^+ \, dy, \tag{64a}$$

where the zonal extent of the integral is extended to $x = x_e$ since $w_1 = 0$ in Region A. Note that (64a) allows $\hat{x}(y)$ to intersect either the northern or western boundary: In the former case, $\hat{y}_n = y_2$ and $\hat{x}(y_2) > x_w^+$, whereas in the latter $\hat{x}(y_2) = x_w^+$ and $\hat{y}_n \leqslant y_2$. Substituting transports (12) and (38a) into (64a), and accounting for transport (39) at the southwestern corner of Region B in the integral along $\hat{y}_s$, gives

$$\mathcal{W}_b = \int^{\hat{x}(y_2)}_{x_w^+} V_1(x, y_2)dx + \left[\frac{\tau_y^x}{\beta}(x_e - \hat{x})\right]^{\hat{y}_n}_{\hat{y}_s} - \mathcal{V}_B(\hat{y}_s)$$
$$- \frac{h_{\min}}{D}\overline{f^{-1}}\frac{\Delta g'}{2}h_{\min}^2 - \frac{h_{\min}}{D}\left[\frac{\tau_y^x}{\beta}(x_e - x_w^+)\right]^{\hat{y}_n}_{\hat{y}_s}, \tag{64b}$$

where $\overline{f^{-1}} = (1/\Delta y)\int^{\hat{y}_n}_{\hat{y}_s} f^{-1} \, dy$ and $\Delta g' = g'(\hat{y}_2) - g'(\hat{y}_s)$. Finally,

$$\mathcal{M}_{in} = \mathcal{W}_b + \mathcal{W}_c^+ = \left[\frac{\tau_y^x}{\beta}(x_e - \hat{x})\right]^{\hat{y}_n}_{\hat{y}_s} - \mathcal{V}_B(\hat{y}_s) - \frac{h_{\min}}{D}\overline{f^{-1}}\frac{\Delta g'}{2}h_{\min}^2$$
$$- \frac{h_{\min}}{D}\left[\frac{\tau_y^x}{\beta}(x_e - x_w^+)\right]^{\hat{y}_n}_{\hat{y}_s}, \tag{65}$$

since the first integral on the right-hand side of (64b) is $-\mathcal{W}_c^+$.

Fig. 7 plots $\mathcal{M}_{in}$ as function of τ_o (red curve). Region B exists ($\gamma_b > 1$) provided that $\tau_0 > \tau_b = 0.056$ N/m^2, with $\mathcal{M}_{in}$ increasing away from this critical value as the area of Region B and w_1 increase. Note also that the curve has a slight bend in slope across τ_c, a consequence of $\hat{x}$ switching from x_w^+ to $\hat{x}(y_2)$ in (65).

5.3. Western-boundary entrainment $\mathcal{W}_w$

Western-boundary-layer entrainment, $\mathcal{W}_w = \int_{\bar{y}_w}^{y_2} W_w dy \equiv \widetilde{\mathcal{W}}_w + \mathcal{W}'_w$, has two components. The first,

$$\mathcal{W}'_w = -\frac{h_{\min}}{D}\frac{\tau_y^x}{\beta}\left(x_e - x_w^+\right), \qquad y = y_2, \tag{66}$$

is due to entrainment by (17a) as the barotropic, western-boundary current of the Subpolar Gyre flows southward across y_2 and layer 1 is formed by surface heating. It is of the order $(h_{\min}/D)\mathcal{M}_n$, small compared to the other overturning transports. The second component, $\widetilde{\mathcal{W}}_w$, due to entrainment by (17b), occurs along the western boundary south of y_2, and it can reach appreciable values.

As τ_o increases, eventually h_w thins to $h_{\min}$ and western-boundary entrainment begins south of y_2 ($\widetilde{\mathcal{W}}_w \neq 0$). Interestingly, for realistic parameter choices $\widetilde{\mathcal{W}}_w$ occurs first at $y = \bar{y}_w$. To see why this property is robust, consider the continuity equation integrated zonally across the basin and from y to y_2,

$$\mathcal{V}_1(y) = -\int_y^{y_2} \widetilde{W}_w dy' - \left(\mathcal{W}'_w + \int_y^{y_2}\int_{x_w^+}^{x_e} w_1 \; dx \; dy'\right), \qquad y \leqslant y_2, \tag{67}$$

where $\mathcal{V}_1 \equiv \int_{x_w}^{x_e} V_1 dx$ is the zonally integrated meridional transport, $\widetilde{W}_w \equiv \int_{x_w}^{x_w^+} w_e \; dx$, and w_1 is known in the interior. Analogous to their western-boundary counterparts in Section 3.3, we define two test transports related to $\mathcal{V}_1 : \mathcal{V}'_1(y)$ given by (67) with $\widetilde{W}_w(y) = 0$; and $\tilde{\mathcal{V}}_1(y) \equiv \int_{x_w^+}^{x_e} V_1 dx + \tilde{\mathcal{V}}_{1w}(y)$, where $\tilde{\mathcal{V}}_{1w}(y)$ is given by (18) with $h_w(y) = h_{\min}$, so that $\tilde{\mathcal{V}}_1(y)$ is the maximum meridional transport that can be sustained by the model at latitude y. It follows that if $\mathcal{V}'_1(y) > \tilde{\mathcal{V}}_1(y)$ western-boundary upwelling ($\widetilde{W}_w > 0$) must occur somewhere in the interval $[y, y_2]$.

Now, suppose that τ_o is initially small enough for $\widetilde{W}_w = 0$ everywhere. As τ_o increases, it follows from the preceding discussion that $\widetilde{W}_w$ will appear first at the latitude where $\tilde{\mathcal{V}}_1(y)$ has a minimum value. We assume that its minimum value occurs far enough south of y_2 for $h_e/D \ll 1$ (verified below). Then, a zonal integration of (8a) from x_w to x_e, with (14a) and $h_w = h_{\min}$ gives

$$\tilde{\mathcal{V}}_1 \approx \frac{g'}{2f}\left(h_e^2 - h_{\min}^2\right) - \frac{\tau^x}{f}(x_e - x_w), \qquad h_1 \ll D, \tag{68}$$

where terms that include factors of h_e/D and $h_{\min}/D$ are neglected. Because $g'h_e^2$ is constant (Eq. (21)), $h_{\min}$ is relatively small, and $\tau^x(y)$ varies much faster than f, changes with latitude of $\tilde{\mathcal{V}}_1$ are dominated by the southward Ekman transport (last term in Eq. (68)), which reaches its maximum just south of $\bar{y}_w$. Since $\widetilde{W}_w = 0$ south of $\bar{y}_w$, $\widetilde{W}_w \neq 0$ first occurs at $y = \bar{y}_w$.

A corollary of this result is that $\widetilde{\mathcal{W}}_w > 0$ only when $h_w(\bar{y}_w) = h_{\min}$ so that $\mathcal{V}_1(\bar{y}_w) = \tilde{\mathcal{V}}_1(\bar{y}_w)$. Evaluating (67) at $\bar{y}_w$ and solving for $\widetilde{\mathcal{W}}_w$, then gives

$$\widetilde{\mathcal{W}}_w = \left[\left(\mathcal{M}_n - \mathcal{M}_{in} - \mathcal{W}'_w\right) - \tilde{\mathcal{V}}_1(\bar{y}_w)\right]\theta(\widetilde{\mathcal{W}}_w), \tag{69a}$$

where $\int_{\bar{y}_w}^{y_2}\int_{x_w^+}^{x_e} w_1 \; dx \; dy' = \mathcal{M}_{in} - \mathcal{M}_n$ because $\bar{y}_w$ is less than $\hat{y}_s$ and y''_e in (65) and (63), repsectively, and

$$\tilde{\mathcal{V}}_1(\bar{y}_w) = \frac{g'}{2f}\left[h_e^2 - h_{\min}^2 - \frac{2}{3D}\left(\zeta h_e^3 - h_{\min}^3\right)\right] - \frac{\tau^x}{f}(x_e - x_w), y = \bar{y}_w. \tag{69b}$$

Eq. (69b) is obtained using (18a) and (24), $\zeta \equiv \left[1 - 2\tau^x(x_e - x_w)/\left(g'h_e^2\right)\right]^3$, the property that $V = V_w = 0$ at $y = \bar{y}_w$, and retaining all terms of order h_1/D for accuracy. According to (69a), western-boundary upwelling exists only when $h_w(\bar{y}_w) = h_{\min}$ and $\widetilde{\mathcal{W}}_w$ is positive; in that case, it is the difference be-

tween $\tilde{\mathcal{V}}_1(\bar{y}_w)$ and the aggregate of all entrainments and detrainments farther to the north. Based on (69a), we introduce the non-dimensional parameter

$$\gamma_a = \frac{\mathcal{M}_n - \mathcal{M}_{in} - \mathcal{W}'_w}{\tilde{\mathcal{V}}_1(\bar{y}_w)}, \tag{70}$$

with $\gamma_a > 1$ indicating that $\widetilde{\mathcal{W}}_w > 0$.

It is noteworthy that when there is western-boundary upwelling, $\mathcal{M}$ is given by (69b). Therefore, $\mathcal{M}$ satisfies the remarkable property that it is *independent* of any of the diapycnal processes in the northern ocean. In other words, as long as there is any western-boundary upwelling, $\mathcal{M}$ is unaffected by the parameterizations of deep-water production and interior entrainment in the northern ocean, depending only on g', H_s (since $h_e \propto H_s$), and τ_o.

Fig. 7 plots $\mathcal{W}_w(\tau_o)$ both for the standard run and when $w_d \neq 0$ (solid/dashed and solid magenta curves, respectively). There are two critical values of τ_o at which $\widetilde{\mathcal{W}}_w$ first becomes active: $\tau_a = 0.072$ N/m^2 for the standard run and 0.046 N/m^2 for the $w_d \neq 0$ solution. For $\tau_o \leqslant \tau_a, \mathcal{W}_w = \mathcal{W}'_w$, which increases linearly from zero at $\tau_o = 0$. For $\tau_a < \tau_o \leqslant \tau_c, \mathcal{W}_w$ increases sharply due to $\widetilde{\mathcal{W}}_w$. Finally, $\mathcal{W}_w$ decreases slowly for $\tau_o > \tau_c$, because $\mathcal{M}_n$ has then reached its maximum and the increase of $-\mathcal{V}_1(\bar{y}_w)$ is overcompensated by the increase in $\mathcal{M}_{in}$ in (69a).

5.4. Transport $\mathcal{M}$

Fig. 7 also plots $\mathcal{M} = \mathcal{M}_n - \mathcal{M}_{in} - \mathcal{W}_w$, a combination of the transports discussed above. Interestingly, in the upper panel $\mathcal{M}(\tau_o)$ reaches a maximum at τ_a both in the standard run (dashed black curve) and in the $w_d \neq 0$ solution (solid black curve). When $\tau_o < \tau_a, \mathcal{M}$ increases with τ_o, because of its effect on $\mathcal{M}_n$. When $\tau_o > \tau_a$, however, $\mathcal{M} = \tilde{\mathcal{V}}_1(\bar{y}_w)$ in (69b), which decreases roughly linearly with τ_o. In the $w_d = 0$ solution, the slope of $\mathcal{M}$ flattens somewhat in the region $\tau_b < \tau_o < \tau_a$, where $\mathcal{M}_{in}$ becomes active and partly compensates for the increase in $\mathcal{M}_n$; this effect is not observable for the solution with $w_d \neq 0$ because $\tau_a < \tau_b$.

Fig. 8 (bottom panel) plots $\mathcal{M}(H_s)$ for the same solutions for which $\mathcal{M}_n(H_s)$ is shown in the top panel. In the solutions with $w_d = 0, \mathcal{M} = \mathcal{V}_1(\bar{y}_w)$ when H_s is small enough for western-boundary entrainment to occur (solid curves; Eq. (69b)). For larger H_s, the $w_d = 0$ profiles flatten markedly (dashed curves): $\mathcal{M}$ increases slightly with H_s until the interior entrainment $\mathcal{M}_{in}$ vanishes at $H_s = H_b$, and thereafter remains at its maximum value, $\mathcal{M}_n - \mathcal{W}'_w$, which is determined by τ^x and independent of H_s (Eqs. (57a) and (66)). Solutions with $w_d \neq 0$ (solid curves) have essentially the same regimes as the $w_d = 0$ solutions, with $\mathcal{M} = \tilde{\mathcal{V}}_1(\bar{y}_w)$ for small H_s. Western-boundary upwelling $\widetilde{\mathcal{W}}_w$ persists for larger H_s than for corresponding $w_d = 0$ solutions, however, because $\mathcal{M}_n$ is larger for $H_s > H_c$ (see top panel). Furthermore, since $\mathcal{M}_n$ does not reach a maximum value (Eq. (58)), $\mathcal{M}$ continues to increase with H_s for $H_s > H_b$. A comparison of the four curves shows that $\mathcal{M}$ decreases with increasing τ_o for smaller H_s because it is in the regime of $\mathcal{M} = \tilde{\mathcal{V}}_1(\bar{y}_w)$ here (Fig. 7); for larger $H_s, \mathcal{M}$ increases with increasing τ_o because it is in the regime of $\mathcal{M} = \mathcal{M}_n - \mathcal{W}'_w$ (Fig. 7).

6. OGCM solutions

In this section, we compare the VLOM solutions to corresponding numerical solutions to an OGCM (MITgcm). As we shall see, the solutions are strikingly similar, indicating that the dynamics contained in VLOM are also the dominant processes at work in the OGCM. There are also secondary differences that arise from processes not included in VLOM.

6.1. Overview

The MITgcm is a numerical-modeling toolbox designed at the Massachusetts Institute of Technology to solve different sets of equations describing the atmosphere, ocean, and climate (Hill and Marshall, 1995; Marshall et al., 1997). In the present study, it is configured to solve a finite-volume form of the standard hydrostatic, Boussinesq, primitive equations on spherical coordinates with a free surface. It uses a flux-limiting, third-order scheme for tracer advection. The C-grid has 36 vertical levels with a uniform resolution of 20 m in the upper 400 m, gradually decreasing to 540 m near the bottom, and its horizontal resolution is $0.5° \times 0.5°$. The parameterization of horizontal mixing is Laplacian, with coefficients $\nu_h = 2 \times 10^4$ m^{2}s^{-1} for viscosity and $\kappa_h = 10^2$ m^2 s^{-1} for diffusion. Neither isopycnal diffusion (Redi, 1982; Cox, 1987) nor thickness diffusion (Gent and McWilliams, 1990) is used, and no mixed-layer parameterization is employed. Coefficients of vertical viscosity and diffusivity are both 10^{-5} m^2 s^{-1} except when the stratification becomes statically unstable, in which case vertical diffusivity is increased to a large value. As in VLOM, salinity is neglected and the equation of state is given by (4).

The MITgcm experiments are designed to be as similar to the VLOM standard run as possible. The ocean basin extends from the equator to 60°N, is 40° wide and 4000 m deep. The model is forced by a surface heat flux

$$Q(x,y,z) = -\frac{T - T^*(x,y)}{\delta t} \theta(z + h_{\min}).$$
(71)

According to (71), Q differs from that in VLOM, (5), in that it acts on a "mixed layer" of thickness $h_{\min} = 100$ m, rather than the entire upper layer. For most solutions, $\delta t = 3$ days, ensuring that the surface temperature stays close to T^*; to test the effects due to temperature advection, solutions are also obtained for larger δt (Section 6.5). The wind stress is (7), and solutions are obtained for $\tau_o = 0$, 0.7, 0.12 and 0.17 Nm^{-2}. We use closed, no-slip conditions at the lateral boundaries. In a sponge layer adjacent to the southern boundary, temperature (density) is strongly relaxed towards an exponential profile,

$$\tilde{T}(z) = T_n + (T_s - T_n) \exp\frac{z + h_{\min}}{\Delta H_s} \theta(-z - h_{\min})$$
$$+ (T_s - T_n) \, \theta(z + h_{\min}),$$
(72)

and solutions are obtained for $\Delta H_s = 100$, 150, 200, 250 and 300 m. The northern boundary of that sponge layer, $y'_s = 10°$N, then corresponds to the southern boundary of the basin along y_s in VLOM. Solutions are integrated for 1100 years at which time they are close to equilibrium, and we analyze the variables averaged over the last 100 years of integration.

6.2. Definitions

To allow a comparison of VLOM and MITgcm solutions, we define a measure for the upper-layer thickness in MITgcm, namely

$$h_1 \equiv \left(2 \int_{-D}^0 \int_{-D}^z \frac{\rho_n - \rho}{\rho_n - \rho_0} \, dz' \, dz\right)^{1/2},$$
(73)

where $\rho_0 = \rho(x, y, 0)$. The tropical eastern-boundary thermocline thickness and the density profiles in the sponge layer are then related by

$$H_s \approx \left[(h_{\min} + \Delta H_s)^2 + \Delta H_s^2\right]^{1/2}.$$
(74)

This choice for h_1 is motivated by the property that the upper-layer, no-flow condition

$$\left(g'h_1^2\right)_y = 0, \quad g' = g(\rho_n - \rho_0)/\rho_n, \quad x = x_e,$$
(75)

holds along the eastern boundary, analogous to (21) for VLOM. See (Schloesser, 2011) for a more detailed discussion of the properties of (73).

There is also a homogeneous layer of thickness h_m along the eastern boundary (upper panels of Fig. 9 below). A condition similar to (75) also holds for h_m, namely,

$$h_{mz} = \frac{h_m}{2} \frac{1}{\rho_A(z) - \rho^*(y)},$$
(76)

where $\rho_A(z)$ is the density below, and $\rho^*(y)$ within the surface layer (Sumata and Kubokawa, 2001; Schloesser et al., 2012). In general, $h_1 \geqslant h_m$, with $h_1 = h_m$ only in case $\rho_{Az} = 0$ (as in VLOM) or where $h_1 = D$.

The strength of the meridional overturning circulation is measured using the meridional streamfunction in temperature (density) space, that is, $\psi^T(y, T) = \int_{x_w}^{x_e} \int_{z_T}^0 v \, dz \, dx$, where z_T is the depth of the T-isotherm. In particular, we define the deep-water formation rate $\mathcal{M}_n \equiv \max(\psi^T)$, and the deep-water export $\mathcal{M} \equiv \max[\psi^T(\bar{y}_w)]$, to compare them to their VLOM counterparts.

6.3. Standard run

To illustrate the interior circulation in the standard run ($\Delta H_s = 100$ m, $\tau_o = 0.12$ Nm^{-2}, and $\delta t = 3$ days), Fig. 9 shows meridional sections of temperature and zonal and vertical velocities, and Fig. 10 provides a map of h_1 determined from (73); they are comparable to the plots of the VLOM standard solution in Figs. 6 and 3, respectively. Fig. 10 also includes upper-ocean transports, $\mathbf{V}_1 \equiv \int_{-h_1}^0 \mathbf{v}_1 \mathrm{dz}$.

As shown in the upper panels of Fig. 9, the eastern-boundary temperature structure adjusts in MITgcm such that the depth-integrated geostrophic transport in the vertically uniform surface layer h_m (magenta curve) vanishes, and isotherms are approximately horizontal below. Furthermore, h_1 (cyan curve) adjusts to the same profile (21) as in VLOM (the theoretical curve is not plotted in Fig. 9 because it is visually indistinguishable from the actual h_1 curve); the patterns of zonal (left panel) and vertical velocities (right panel) are quite similar as well. This striking response is independent of the zonal wind forcing, and is the same as discussed in Sumata and Kubokawa (2001) and Schloesser et al. (2012).

The sections at 20°E in the lower panels of Fig. 9 illustrate that isotherms and h_1 are depressed in the Subtropical Gyre from 15°N $\leqslant y \leqslant$ 35°N, and raised in the Subpolar Gyre for 35°N $\leqslant y \leqslant$ 55°N. As in Region A for the VLOM solutions, the zonal current is mostly confined to the upper layer, and flows in the direction of the gyre circulation (compare to Fig. 6). There is also a region in the Subpolar Gyre (42°N $\lesssim y \lesssim$ 44°N) where h_1 is near $h_{\min}$ and the flow extends over the entire water column, as in Region B for VLOM. Furthermore, in the northern part of the Subpolar Gyre, the thermal-wind shear has about the same strength as the gyre flow, so that the flow is eastward near the surface. The maps of layer thickness for the MITgcm (Fig. 10) and VLOM solution (Figs. 3 and 4) have the same basic features, including the eastward extent of Region B. A northern-boundary layer just south of y_2 is apparent in Fig. 10, where U_1 is opposite to the direction of the Sverdrup circulation, suggesting that Rossby waves are damped by a mechanism similar to w_d in VLOM (upper-middle left panel of Fig. 4).

Vertical velocities, and isotherms along the western boundary are shown in Fig. 11. In the Subpolar Gyre ($y > \bar{y}_w = 35°$), all isotherms are near $h_{\min}$ before they outcrop, and relatively strong upwelling occurs. South of $\bar{y}_w$, upwelling weakens, and and the coastal h_1 deepens abruptly as in VLOM, where these properties are ensured through the stepfunction in (17b).
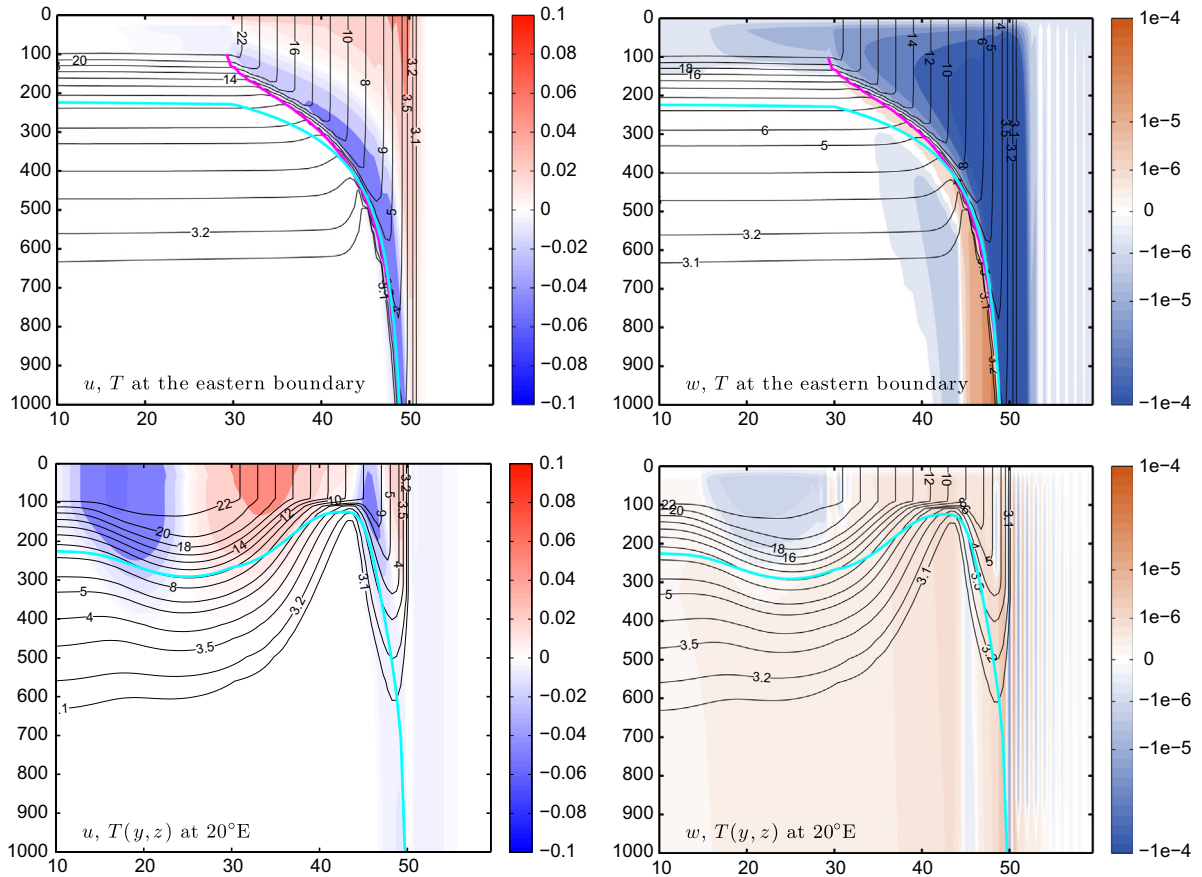
Fig. 9. Meridional sections from the MITgcm run with τ_o = 0.12 N/m², ΔH_s = 100 m (H_s = 223 m) and δt = 3 days after 1000 years of integration showing temperature (contours) and velocities (shading). The upper-left panels show zonal velocities one grid point away from (left) and vertical velocities at (right) the eastern boundary. The lower panels show the same variables in the interior ocean at 20°E. Cyan lines indicate h_1 defined by Eq. (73), and the magenta lines the homogeneous layer thickness defined by (76). (For interpretation of the references to colour in this figure legend, the reader is referred to the web version of this article.)
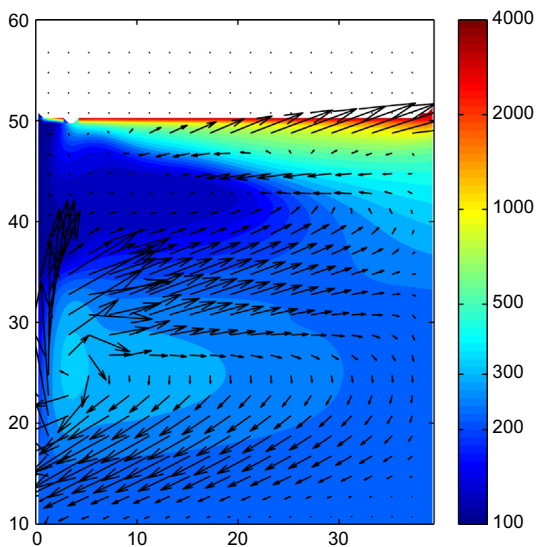

Fig. 10. Map of layer thickness h_1 and $\boldsymbol{V}_1$ in the MITgcm solution with τ_o = 0.12 N/m², ΔH_s = 100 m (H_s = 223 m), and δt = 3 days.

Despite these many similarities, the MITgcm solution also exhibits (secondary) features not explained by our VLOM solutions. A flow-pattern somewhat similar to the Stommel and Arons (1960) circulation develops below the wind-driven upper-layer flow,

which is characterized by northward flow at depth and weak, interior upwelling (lower-right panel in Fig. 9). As suggested by Schloesser et al. (2012), the upwelling in the deep layer is strongest at the eastern boundary, where a sharp thermocline is maintained by the upper-ocean sinking and fast Kelvin-wave response. We also find that thermocline slopes are slightly flatter in MITgcm than predicted by VLOM, and hence that Region B is slightly smaller in the MITgcm. These features are attributable to the interior diffusion in MITgcm, and qualitatively similar features arise in VLOM when diffusion in the form of a $w_1 = w_m = \kappa/h_1$ is included (e.g., Schloesser et al., 2012).

6.4. Overturning strength

Fig. 8 plots data points for $\mathcal{M}_n(H_s)$ and $\mathcal{M}(H_s)$ from a number of MITgcm solutions with different H_s and τ_o values. As in VLOM, $\mathcal{M}_n$ is nearly independent of τ_o for the experiments with H_s = 223 m, but the difference among them increases as H_s increases. Overall, the agreement between the two models is very good, supporting the conclusion that the processes causing the diapycnal overturning are similar between the two models.

The strength of the deep-water export $\mathcal{M}$ is shown in the lower panel of Fig. 8. Regardless of the strength of the winds, $\mathcal{M}$ increases with thermocline thickness H_s. Because $\mathcal{M}$ increases faster with H_s for stronger winds, however, $\mathcal{M}$ decreases (increases) with τ_o for small (large) H_s. These general properties are the same as in the VLOM solutions. The agreement between $\mathcal{M}$ in MITgcm and VLOM is particularly good when H_s is relatively shallow. A possible
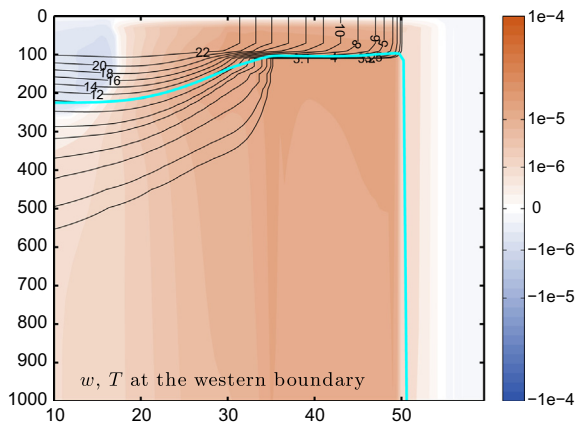
Fig. 11. Temperature and vertical velocity along the western boundary in the MITgcm solution with $\tau_o = 0.12$ N/m^2, $\Delta H_s = 100$ m ($H_s = 223$ m), and $\delta t = 3$ days. The cyan curve indicates h_1 defined by (73). (For interpretation of the references to colour in this figure legend, the reader is referred to the web version of this article.)

explanation for the discrepancy at larger H_s values is diffusive mixing, which provides another "shortcut" (other than wind-driven upwelling in the interior ocean and western-boundary upwelling) for the MOC in the Subpolar Gyre in the MITgcm, and is not included in VLOM.

6.5. Solutions with large δt

All prior solutions assume that δt is small, thereby eliminating surface temperature advection as a significant process. To demonstrate that this restriction does not severely affect our conclusions, we obtained a test solution in which $\delta t = 50$ days and with other parameters the same as for the standard run. In the test, the near-surface temperature field deviates significantly from T^* in the standard run, with the line $y_2(x)$ where surface temperature first decreases to its coldest value shifted north about 2–3°. Nevertheless, the overturning transports are $\mathcal{M}_n = 6.8$ Sv and $\mathcal{M} = 2.4$ Sv in the test, close to their values in the standard run ($\mathcal{M}_n = 7.0$ Sv and $\mathcal{M} = 2.4$ Sv) and consistent with values in VLOM when y_2 is shifted northward similarly. When δt is relaxed further, however, advection becomes so strong that finally the coldest surface temperature, and hence the deep-ocean temperature, is no longer prescribed but internally determined by the model (e.g., Park and Bryan, 2000).

The above tests do not fully explore the possible effects of advection. For example, it is known that the effect of density advection increases when the meridional flow is concentrated in an eastern-boundary current over a continental slope (e.g., Spall and Pickart, 2001). Furthermore, understanding the full impact of density advection requires fresh-water forcing to be included in the model. A consideration of either of these processes is beyond the scope of this paper.

7. Applications

In this section, we apply VLOM to solutions that differ from the standard run in two key aspects: In the first case, the Subpolar Gyre does *not* extend into the northern part of the basin, where $T_1 = T_n$ (i.e., $y_{2w} < y_2$ or $\tau^x = 0$). Second, solutions are forced by a prescribed overturning rate, $\mathcal{M}$, rather than by a layer thickness H_s at the southern boundary. Besides allowing for our results to be directly related to some previous studies, these examples demonstrate the robustness of the relations between thermocline depth, overturning circulation and wind and buoyancy forcing in VLOM.

7.1. Solutions with $y_{2w} < y_2$ and $\tau^x = 0$

The solutions in Sections 3 and 4 illustrate how northward flow in the Subpolar Gyre can generate the surface convergence needed to establish the MOC downwelling branch. In the real ocean and OGCM solutions, however, MOC deep-water formation also occurs *north* of the Subpolar Gyre, such as in the GIN Seas. An analogous situation in our model occurs when $y_{2w} < y_2$, in which case there is no flow across y_2 and hence $\mathcal{W}_c^\pm = 0$.

If $y_{2w} < y_2$ and $w_d = 0$, there is no mechanism left for water to detrain in the northern ocean; consequently, $\mathcal{M}_n = 0$ and no MOC descending branch can be established in the north. On the other hand, water can still upwell in Region B if $\gamma_b > 1$, in which case a "reversed" MOC ($\mathcal{M} < 0$) flows southward across the open boundary. This solution then resembles that in the Tsujino and Suginohara (1999) model (Section 1), in which water that upwells due to Ekman suction in the northern hemisphere downwells in the southern hemisphere. If $w_d \neq 0$, a northern sinking branch with $\mathcal{M}_n = -\mathcal{W}_d$ is established as shown in the lower panels of Fig. 4. The MOC is still affected by the wind forcing, however, if upwelling in the interior of the Subpolar Gyre ($\mathcal{M}_{in}$) or in the western-boundary layer ($\mathcal{W}_w$) occurs. As in the standard run, these processes then provide a shortcut for the MOC, and $\mathcal{M}$ is reduced south of $\bar{y}_w$.

In the limit that $\tau^x = 0$, the wind-driven circulation disappears from our solutions, and hence they are an extreme example of the case with $y_{2w} < y_2$. They are similar to the solutions discussed in Schloesser et al. (2012), except the Schloesser et al. (2012) solutions are closed by diffusive upwelling ($w_m \neq 0$) within the northern hemisphere. Interestingly, when $w_d = 0$, the response is a state of rest, even though the meridional density and pressure difference remain unchanged; the response is the same as the no-MOC solution with $w_m = 0$ discussed in Schloesser et al. (2012).

7.2. Solutions forced by $\mathcal{M}$

In all previous solutions, we have assumed that the eastern-boundary layer thickness H_s is prescribed, and solved for the resulting overturning strength, $\mathcal{M}$. The same steady-state solution results if $\mathcal{M}$ is prescribed by external processes in the South Atlantic (e.g., wind-driven upwelling in the Southern Ocean; Toggweiler and Samuels, 1995) and H_s responds to that forcing (Schloesser et al., 2012).

Since in a steady state, the solution is indistinguishable from a corresponding solution with a prescribed H_s, the same relations for $\mathcal{M}(H_s)$ and its components hold as derived in Section 5. Thus, Fig. 8 also provides $H_s(\mathcal{M})$, that is, gives the eastern-boundary layer thickness H_s that results from a prescribed $\mathcal{M}$. From this perspective, it is clear that if $\mathcal{M}$ is externally specified (e.g., by Southern Ocean winds as in Wyrtki, 1961; Toggweiler and Samuels, 1995; Samelson, 2009), the thermocline depth throughout the basin is determined.

When $\mathcal{M}$ is fixed, H_s depends on τ_o. To illustrate this dependence, Fig. 12 plots $H_s(\tau_o)$ for a solution with the same parameter values as in the standard run, $w_d \neq 0$, $h_{max} = 3H_s$, and $\mathcal{M} = 10$ Sv. For reference, the figure also provides the interior ($\mathcal{M}_{in}$) and western-boundary entrainment ($\tilde{\mathcal{W}}_w$), as well as critical wind strengths τ_a, τ_b and τ_c. For $\tau_o \leqslant \tau_a$, no entrainment occurs (i.e., $\tilde{\mathcal{W}}_w = \mathcal{M}_{in} = 0$), and hence $\mathcal{M} = \mathcal{M}_n - \mathcal{W}_w' \approx \mathcal{M}_n = -\mathcal{W}_d - \mathcal{W}_c^-$ (Section 5); consequently, H_s decreases as τ_o increases, such that the increase in wind-driven convergence ($\mathcal{W}_c^-$) is balanced by a decrease in convergence caused by detrainment ($\mathcal{W}_d$). When $\tau_o > \tau_a, \tilde{\mathcal{W}}_w > 0$ and hence $\mathcal{M} = \tilde{\mathcal{V}}_w(\bar{y}_w)$; in that case, H_s is determined by inverting (69b), and has to increase with τ_o. Thus, when τ_o increases further, such that $\mathcal{M}_{in} > 0$ for $\tau_o > \tau_b$, and finally $\tau_o > \tau_c$, such that $\mathcal{M}_n$ becomes independent of τ_o (i.e., $\gamma_c < 1$), H_s is no longer affected by the diapycnal processes in the subpolar ocean. The

finding that $(H_s)_{\tau_o} \lessgtr 0$ for $\tau_o \gtrless \tau_a$ is consistent with $(\mathcal{M})_{\tau_o} \gtrless 0$ for $\tau_o \gtrless \tau_a$ (Fig. 7), because $(\mathcal{M})_{H_s} > 0$ (Fig. 8, $w_d \neq 0$).

8. Summary and discussion

A hierarchy of solutions to models of different complexity has been developed to investigate the dynamics of the deep, meridional overturning circulation (MOC). Recently, Schloesser et al. (2012) explored solutions at the base of that hierarchy, forced only by a surface buoyancy flux. In their study, a variable-density, 2-layer model (VLOM) proved to be a useful tool to identify key processes that establish the descending branch of the MOC. Here, we extend that study to include wind forcing: The near-surface circulations in all the solutions now in our hierarchy are illustrated in Fig. 13. Collectively, they provide a general theory that relates MOC strength and structure to the thermocline depth in the eastern, tropical ocean, the meridional surface-density difference, mixing processes, and zonal wind forcing.

Model and experimental design: We obtain analytic solutions to VLOM in an idealized, flat-bottom basin in the northern hemisphere. Because density depends only on temperature, and the equation of state is linear, density and temperature are essentially equivalent. The southern boundary is open, and solutions are derived for a prescribed southeastern upper-layer thickness, H_s. This southern-boundary closure does not affect the generality of our equilibrium solutions: The relation between H_s and the mass flux across the southern boundary $\mathcal{M}$, as determined by the descending branch of the MOC, holds regardless of the southern-boundary condition. To demonstrate this point, we also discuss solutions where $\mathcal{M}$ is prescribed, rather than H_s (Section 7.2). In more complete (closed) models of the MOC, a second relation relating $\mathcal{M}$ to H_s is determined by the physics of the upwelling branch, and equilibrium solutions are then found by matching both relations (Gnanadesikan, 1999; Schloesser et al., 2012).

The model is forced by a surface heat flux Q, which instantly relaxes near-surface temperature to a prescribed $T^*(y)$ that decreases linearly from a maximum T_s south of $y_1 = 30°N$ to the deep-ocean temperature T_n at $y_2 = 50°N$. North of y_2, then, the upper layer vanishes and the model ocean simplifies to a 1-layer system. The model is also forced by westerly winds, which drive a Subtropical and a Subpolar Gyre. In most solutions, the Subpolar Gyre extends north

of y_2 (i.e., $y_{2w} > y_2$), in which case it impacts the MOC downwelling branch.

To generate an MOC, several processes are included in the model to allow mass to transfer between the two layers. These processes are specified as across-interface velocities, $w_1 = w_e + w_c + w_d$: w_e represents mixed-layer processes that prevent h_1 from becoming smaller than a minimum thickness h_{min} by entraining water into layer 1 (Nonaka et al., 2006); w_c allows mass to transfer from layer 1 into layer 2 when water flows northward across y_2 and hence is cooled to T_n by Q, and vice versa; finally, w_d represents mixing processes that prevent h_1 in the interior ocean from becoming thicker than a maximum thickness h_{max} by restratifying the water column (Fox-Kemper et al., 2008; Schloesser et al., 2012).

VLOM solutions: We obtain solutions with and without w_d, and for $y_{2w} \gtrless y_2$, and for each of the solutions we vary the wind strength τ_o. In most cases, there are three critical values of τ_o, as measured by the non-dimensional parameters, γ_a, γ_b, and γ_c, above which solutions change their character: upwelling begins at the western boundary ($\gamma_a > 1$); $h_1 = h_{min}$ in the interior ocean (Region B; $\gamma_b > 1$); and the boundary of Region B intersects y_2 ($\gamma_c > 1$).

Solutions with $w_d = 0$ and $y_{2w} > y_2$: Our standard solution assumes that $w_d = 0$, that is, there is no process that allows detrainment across the bottom of layer 1; as a result, w_c is the only process that can generate the MOC downwelling branch (Section 3). Along the eastern boundary, h_1 thickens poleward in response to the surface temperature gradient, a consequence of the no-normal-flow boundary condition, which requires cancelation of the depth-integrated, alongshore pressure gradient. Just south of y_2, h_1 extends over the entire water column, before it outcrops and vanishes farther to the north. This eastern-boundary structure (Eq. (21)) is equivalent to that discussed in Sumata and Kubokawa (2001) and Schloesser et al. (2012).

In the interior ocean, Rossby waves adjust the layer interface such that the interior-ocean Sverdrup transport is entirely contained in the upper layer, and the deep layer is at rest (Region A). As in corresponding isopycnal layer model solutions (Huang, 1986; Huang and Flierl, 1987; Nonaka et al., 2006), a region where layer 1 outcrops ($h_1 = h_{min}$; Region B) can exist in the western part of the subpolar ocean if τ_o is sufficiently strong ($\gamma_b > 1$). Within Region B, Ekman suction in layer 1 is balanced by entrainment w_e, and the geostrophic part of the Sverdrup transport is evenly
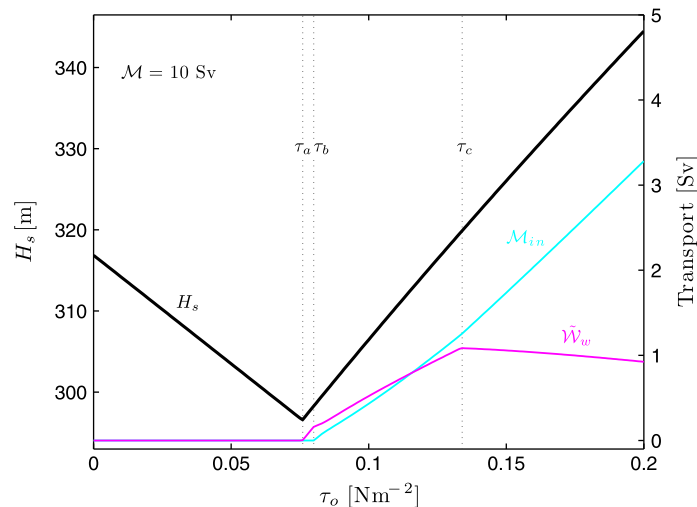

Fig. 12. Eastern-boundary layer thickness, H_s (black curve), in VLOM as a function of wind strength, τ_o, in solutions with a prescribed transport across the southern boundary of $\mathcal{M} = 10$ Sv. Other parameters are as in the standard run, with $w_d \neq 0$ and $\tilde{h}_{max} = 3H_s$. Interior ($\mathcal{M}_{in}$; cyan curve) and western-boundary entrainment ($\tilde{\mathcal{W}}_w$; magenta curve) are also shown for reference. The critical wind strength τ_a indicates whether $\tilde{\mathcal{W}}_w = 0$ ($\tau_o \leqslant \tau_a$) or $\tilde{\mathcal{W}}_w > 0$ ($\tau_o > \tau_a$), τ_b indicates whether $\mathcal{M}_{in} = 0$ ($\tau_o \leqslant \tau_b$) or $\mathcal{M}_{in} > 0$ ($\tau_o > \tau_b$), and τ_c whether $\gamma_c < 1$ ($\tau_o < \tau_c$) or $\gamma_c \geqslant 1$ ($\tau_o \geqslant \tau_c$). (For interpretation of the references to colour in this figure legend, the reader is referred to the web version of this article.)
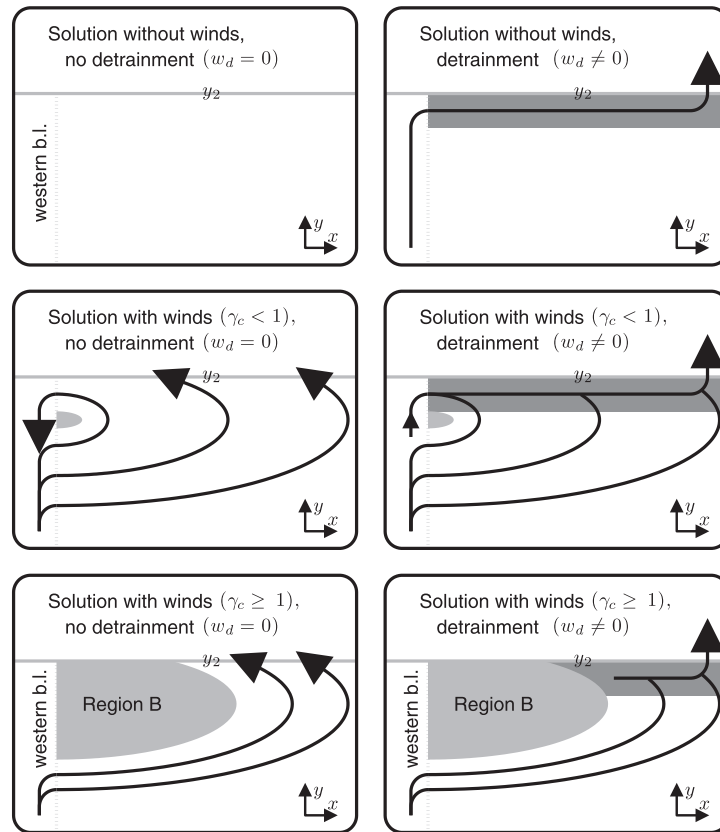
Fig. 13. Schematic maps of layer-1 flow in the subpolar ocean with (right panels) and without restratification process w_d (left panels). The top panels show the circulation in solutions without winds, the middle panel with winds and $\gamma_c < 0$, and the bottom panels with winds and $\gamma_c \geqslant 1$. Region B, where $h_1 = h_{min}$ and $w_e > 0$, is indicated by light shading, and Region N by dark shading.

distributed over the entire water column. Interestingly, if τ_o is strong enough for the eastern edge of Region B, $\hat{x}(y)$, to intersect y_2 ($\gamma_c > 1$), h_1 isolines and Rossby-wave characteristics in the Subpolar Gyre converge to a single point $[\hat{x}(y_2), y_2]$.

Since $w_d = 0$, the MOC downwelling branch occurs entirely by w_c, that is, when layer-1 water within the Subpolar Gyre flows northward across y_2; at that latitude, layer 1 disappears (since T_1 is cooled to T_2) and hence layer-1 water necessarily detrains into layer 2 (middle-left and bottom-left panels of Fig. 13). When Region B intersects y_2 ($\gamma_c > 1$), the detrainment occurs entirely east of $\hat{x}(y_2)$ (middle-left panel of Fig. 13). This downwelling mechanism differs fundamentally from that in previous idealized models, in which downwelling occurs across the bottom of the upper layer (*e.g.*, Luyten and Stommel, 1986; Pedlosky and Spall, 2005; Schloesser et al., 2012), and the associated w drives the meridional near-surface flow, V_1. Here, V_1 is entirely driven by Ekman pumping, which, in concert with Q, forces the geostrophic flow to cross isopycnal surfaces.

The circulation is closed in a western-boundary layer, where we solve for the boundary-current transport $\mathcal{V}_{1w}(y)$ and entrainment transport $W_w(y)$ by integrating the zonally integrated continuity equation southward from y_2, in the direction of Kelvin-wave propagation. Western-boundary entrainment becomes necessary when the wind forcing is strong enough for the interior circulation in the Subpolar Gyre to draw more water from the boundary layer than can be supplied by the surface branch of the boundary current ($\gamma_a \geqslant 1$). When τ_o increases until entrainment begins (γ_a becomes greater than 1), for typical model parameters it does so first at the gyre boundary $y = \bar{y}_w$, and for larger τ_o spreads northward to fill the entire subpolar western-boundary region. By assumption, there is no entrainment in the subtropics, either in the interior

ocean or western-boundary layer. The boundary-current transport remains constant south of the Subtropical Gyre and across the southern boundary, forming a large-scale MOC.

Solutions with $w_d \neq 0$ and $y_{2w} > y_2$: When detrainment $w_d \neq 0$, solutions are altered in a northern-boundary layer (Region N) adjacent to y_2 (Section 4). In the limit that $t_d \rightarrow 0$, h_1 relaxes to h_{max} instantly, and so w_d is only active in a narrow eastern-boundary layer ($x_e^- \leqslant x \leqslant x_e$). The circulation in this eastern-boundary layer is not affected by the wind, and hence is the same as described by Schloesser et al. (2012). West of the eastern-boundary layer, layer-2 potential vorticity is conserved throughout the interior of Region N. Because $h_1(x_e^-) = h_{max}$ is constant and f does not change much in Region N, $h_1 \lesssim h_{max}$ throughout Region N, and the geostrophic part of the Sverdrup flow is almost evenly distributed over the water column. In addition, the surface density gradient drives an eastward current in layer 1 that converges to the eastern boundary; there, layer-1 water detrains into layer 2, and returns to the interior ocean in layer 2. If the focal point of Rossby-wave characteristics exists inside the domain ($\gamma_c \geqslant 1$), w_d affects the circulation only within Region N and does not impact the transport of the large-scale MOC (bottom-right panel of Fig. 13). If $\gamma_c < 1$, however, the flow in Region N connects to the western-boundary current, and so does impact the MOC transport (middle-right panel of Fig. 13).

Solutions with $y_{2w} < y_2$: When the Subpolar Gyre does not extend into the homogeneous part of the ocean ($y_{2w} < y_2$), w_d is the only mechanism by which water can detrain. With $w_d \neq 0$, the sinking branch is established entirely by Rossby-wave damping, as in solutions without wind forcing (Section 7; Schloesser et al., 2012; top-right panel of Fig. 13). With $w_d = 0$, no detrainment can occur within the model domain, and so the model cannot generate am MOC with a northward surface branch ($\mathcal{M} > 0$; top-left

panel of Fig. 13). On the other hand, if there is wind-driven upwelling in the northern ocean ($\gamma_b \geqslant 1$), a "reversed" MOC is formed ($\mathcal{M} < 0$), with southward upper-layer flow across the southern boundary of the model domain and the MOC descending branch located in the southern hemisphere, as in the solutions of Tsujino and Suginohara (1999).

Overturning transports: A strength of VLOM is that it allows for relatively simple, analytic expressions for the rate of deep-water formation, $\mathcal{M}_n$ (Section 5). In most cases, our results recover (1) in that $\mathcal{M}_n$ is (roughly) proportional to the meridional pressure difference (*e.g.*, Park and Bryan, 2000). On the other hand, because the processes that generate detrainment are somewhat different in VLOM than in previous idealized models and scalings, the proportionality function C in (1) has a different form. When the descending branch is well separated from the western-boundary layer in the subpolar ocean ($\gamma_c > 1$), C depends on the relative strength of the Ekman and Sverdrup transports across the outcropping latitude y_2, as in (57b). Interestingly, (57b) is independent of the presence of detrainment w_d when $\gamma_c > 1$: If w_d is included, the detrainment by w_c is reduced by the same amount that is generated by w_d. The deep-water formation rate is affected by w_d, however, when Region N extends to the western boundary ($\gamma_c < 1$), as given by (63). As a result, $\mathcal{M}_n$ then also depends on the strength of the Rossby-wave damping ($h_{\max}$) in the northern-boundary layer, and it has a slightly different form than (1). When the Subpolar Gyre does not extend into the homogenous part of the ocean ($y_{2w} < y_2$), such that detrainment occurs *only* by w_d, $\mathcal{M}_n$ is independent of the winds, the same as in Schloesser et al. (2012).

Upwelling occurs in the Subpolar Gyre when the layer interface outcrops in the interior ocean (Tsujino and Suginohara, 1999; Nonaka et al., 2006). It can also occur in the western-boundary layer, and may be of the same order as the deep-water formation rate, $\mathcal{M}_n$. Because these upwellings provide a "shortcut" for the MOC, the export of deep water from the subpolar ocean, $\mathcal{M}$, defined as the formation rate minus the total upwelling in the subpolar ocean, constitutes a better measure for the strength of the large-scale MOC in our model. Remarkably, however, in some of our solutions $\mathcal{M}$ is independent of the diapycnal processes occurring within the Subpolar Gyre (*e.g.*, $\mathcal{M}_n$), namely, when western-boundary upwelling occurs at the boundary between the two gyres, $\bar{y}_w$. In that case, $\mathcal{M} = \tilde{\mathcal{V}}_{1w}(\bar{y}_w)$ (Eq. (69b)) is the maximum meridional transport that can be sustained by the model across $\bar{y}_w$, and hence determined by local processes (geostrophy and Ekman transport). For example, if $\mathcal{M}_n$ is increased by increasing wind curl near y_2, the western-boundary upwelling just north of $\bar{y}_w$ also increases in such a way that $\mathcal{M}$ remains unchanged.

OGCM solutions: We validate our analytic theory by comparing VLOM solutions to corresponding solutions to an OGCM (MITgcm; Section 6). Despite its simplicity and limited vertical resolution, VLOM reproduces many features of the three-dimensional circulation in MITgcm, and there is a relatively good correspondence between the strength of overturning in the two models (Fig. 8). From these similarities, we conclude that the physical mechanisms that control the MOC in VLOM are also at work in a fundamental way in more realistic models.

The temperature relaxation time scale is extended to $\delta t = 50$ days in one of our MITgcm experiments, such that the surface heat flux Q is weak enough for surface temperatures to be influenced by advection. Somewhat surprisingly, the solution does not change much, the most apparent difference being that outcropping lines are shifted somewhat farther to the north in the Subpolar Gyre. Even in this case, then, the large-scale MOC is still determined by the same dynamical processes identified in VLOM. We note, however, that the above test is insufficient to fully explore the possible effects of advection. For example, it is known that the effect of density advection increases when the meridional flow is concentrated over topography. Moreover, a more comprehensive understanding of the impact of advection requires fresh-water forcing to be included in the model. A consideration of either of these processes is beyond the scope of this paper.

Variability: Although our model is steady state, our solutions are still useful for interpreting long-term (quasi-steady) changes in the AMOC. For example, Lozier et al. (2010) recently noted that changes in AMOC strength over the past 50 years did not occur coherently throughout the North Atlantic, with the AMOC weakening in the subtropics and strengthening in the subpolar region. Our model cannot explain the weakening of the large-scale, subtropical AMOC transport, since solutions are externally forced by prescribing H_s (or $\mathcal{M}$). It can, however, provide a possible explanation for the *relative* changes between the subpolar and subtropical overturning strengths, which are consistent with an increase of the westerlies in our VLOM solutions. Consider the case with western-boundary upwelling ($\gamma_a > 1$). The subtropical overturning strength ($y \leqslant \bar{y}_w$) is then given by $\mathcal{M} = \tilde{\mathcal{V}}_1(\bar{y}_w)$. Recall that $\tilde{\mathcal{V}}_1(\bar{y}_w)$ changes with τ_o roughly like the zonally integrated Ekman transport across $\bar{y}_w$ (Eq. (69b)) so that a strengthening of the westerlies implies a weakening of $\mathcal{M}$. At the same time, the strengthened winds increase the Subpolar Gyre circulation, and $\mathcal{M}_n$ either remains constant ($\gamma_c > 1$) or increases ($\gamma_c < 1$). While the impact of varying winds on salinity advection towards high latitudes (not included in VLOM) has been emphasized (*e.g.*, Häkkinen et al., 2011), our solutions also suggest a more direct control of the AMOC structure in the North Atlantic, somewhat consistent with the numerical experiments of Biastoch et al. (2008).

In conclusion, our overall goal is to derive a hierarchy of MOC models that is as complete as possible, one that fills gaps in the existing one. In the current study and in Schloesser et al. (2012), we have explored the effects of surface density and wind forcing in detail. Nevertheless, our models still lie near the bottom of a hierarchy that extends to real-world simulations. In future studies, we hope to include processes associated with bottom topography, realistic basin geometry, time-dependent forcing, and surface density advection within our idealized modeling framework.

Acknowledgments

References

Biastoch, A., Böning, C.W., Getzlaff, J., Molines, J.-M., Madec, G., 2008. Causes of interannual–decadal variability in the meridional overturning circulation of the midlatitude North Atlantic ocean. Journal of Climate 21, 6599–6615.

Bryan, F., 1986. High-latitude salinity effects and interhemispheric thermohaline circulations. Nature 323, 301–304.

Bryan, F., 1987. On the parameter sensitivity of primitive equation ocean general circulation models. Journal of Physical Oceanography 17, 970–985.

Bryan, K., Cox, M.D., 1967. A numerical investigation of the oceanic general circulation. Tellus 19, 54–80.

Cessi, P., Wolfe, C.L., 2009. Eddy-driven buoyancy gradients on eastern boundaries and their role in the thermocline. Journal of Physical Oceanography 39, 1596–1614.

Cox, M.D., 1987. Isopycnal diffusion in a z-coordinate ocean model. Ocean Modelling 74, 1–5.

De Boer, A.M., Gnanadesikan, A., Edwards, N.R., Watson, A.J., 2010. Meridional density gradients do not control the Atlantic overturning circulation. Journal of Physical Oceanography 40, 368–380.

Dewar, W.K., 1991. Arrested fronts. Journal of Marine Research 49, 21–52.

Dewar, W.K., Samelson, R.M., Vallis, G.K., 2005. The ventilated pool: a model of subtropical mode water. Journal of Physical Oceanography 35, 137–150.

Fox-Kemper, B., Ferrari, R., Hallberg, R., 2008. Parameterization of mixed layer eddies. Part I: Theory and diagnosis. Journal of Physical Oceanography 38, 1145–1165.

Ganachaud, A., Wunsch, C., 2000. Improved estimates of global ocean circulation, heat transport and mixing from hydrographic data. Nature 408, 453–456.

Gent, P.R., McWilliams, J.C., 1990. Isopycnal mixing in ocean general circulation models. Journal of Physical Oceanography 20, 150–155.

Gnanadesikan, A., 1999. A simple predictive model for the structure of the oceanic pycnocline. Science 283, 2077–2079.

Häkkinen, S., Rhines, P., Worthen, D.L., 2011. Warm and saline events embedded in the meridional circulation of the northern North Atlantic. Journal of Geophysical Research, 116.

Hill, C., Marshall, J., 1995. Application of a parallel Navier–Stokes model to ocean circulation in parallel computational fluid dynamics. In: Proceedings of Parallel Computational Fluid Dynamics: Implementations and Results Using Parallel Computers, pp. 545–552.

Huang, R.X., 1986. Numerical simulation of a wind-driven circulation in a subtropical/subpolar basin. Journal of Physical Oceanography 16, 1636–1650.

Huang, R.X., Flierl, G.R., 1987. Two-layer models for the thermocline and current structure in subtropical/subpolar gyres. Journal of Physical Oceanography 17, 872–884.

Kawase, M., 1987. Establishment of deep ocean circulation driven by deep water production. Journal of Physical Oceanography 17, 2294–2317.

Klinger, B.A., Drijfhout, S., Marotzke, J., Scott, J.R., 2004. Remote wind-driven overturning in the absence of the Drake Passage effect. Journal of Physical Oceanography 34, 1036–1049.

Lozier, M., Roussenov, V., Reed, M.S.C., Williams, R.G., 2010. Opposing decadal changes for the north atlantic meridional overturning circulation. Nature Geoscience 3, 728–734.

Luyten, J.R., Pedlosky, J., Stommel, H., 1983. The ventilated thermocline. Journal of Physical Oceanography 13, 292–309.

Luyten, J.R., Stommel, H., 1986. Gyres driven by combined wind and buoyancy flux. Journal of Physical Oceanography 16, 1551–1560.

Marotzke, J., 1997. Boundary mixing and the dynamics of three-dimensional thermohaline circulations. Journal of Physical Oceanography 27, 1713–1728.

Marotzke, J., Scott, J.R., 1999. Convective mixing and the thermohaline circulation. Journal of Physical Oceanography 29, 2962–2970.

Marotzke, J., Willebrand, J., 1991. Multiple equilibria of the global thermohaline circulation. Journal of Physical Oceanography 21, 1372–1385.

Marshall, J., Adcroft, A., Hill, C., Perelman, L., Heisey, C., 1997. A finite-volume, incompressible Navier Stokes model for studies of the ocean on parallel computers. Journal of Geophysical Research, 5753–5766.

Munk, W., Wunsch, C., 1998. Abyssal recipes II: Energetics of tidal and wind mixing. Deep-Sea Research Part I 45, 1977–2010.

Munk, W.H., 1950. On the wind-driven ocean circulation. Journal of Meteorology 7 (2), 79–93.

Nonaka, M., McCreary, J.P., Xie, S.-P., 2006. Influence of midlatitude winds on the stratification of the equatorial thermocline. Journal of Physical Oceanography 36, 222–237.

Park, Y.-G., Bryan, K., 2000. Comparison of thermally driven circulations from a depth coordinate model and an isopycnal model, Part I: A scaling law and sensitivity to vertical diffusivity. Journal of Physical Oceanography 30, 590–605.

Parsons, A.T., 1969. A two-layer model of Gulf Stream separation. Journal of Fluid Mechanics 39 (3), 511–528.

Pedlosky, J., Spall, M.A., 2005. Boundary intensification of vertical velocity in a β-plane basin. Journal of Physical Oceanography 35, 2487–2500.

Radko, T., Kamenkovich, I., 2011. Semi-adiabatic model of the deep stratification and meridional overturning. Journal of Physical Oceanography 41, 757–780.

Redi, M.H., 1982. Oceanic isopycnal mixing by coordinate rotation. Journal of Physical Oceanography 12, 1154–1158.

Rhines, P.B., 1986. Vorticity dynamics of the ocean general circulation. Annual Review of Fluid Mechanics 18, 433–497.

Robinson, A., Stommel, H., 1959. The oceanic thermocline and the associated thermohaline circulation. Tellus 11, 295–308.

Samelson, R.M., 2009. A simple dynamical model of the warm-water branch of the middepth meridional overturning cell. Journal of Physical Oceanography 39, 1216–1230.

Sandström, J.W., 1916. Meteorologische Studien im schwedischen Hochgebirge. Göteborgs K. Vetensk. Vitterhetssamhällets Handkl. 27, 48.

Schloesser, F., 2011. On the dynamics of the Atlantic meridional overturning circulation in idealized models forced by differential heating and winds. Ph.D. thesis, University of Hawaii at Manoa.

Schloesser, F., Furue, R., McCreary, J.P., Timmermann, A., 2012. Dynamics of the Atlantic meridional overturning circulation. Part 1: Buoyancy-forced response. Progress in Oceanography 101 (1), 33–62.

Spall, M.A., 2010. Dynamics of downwelling in an eddy-resolving convective basin. Journal of Physical Oceanography 40, 2341–2347.

Spall, M.A., Pickart, R.S., 2001. Where does dense water sink? A subpolar gyre example. Journal of Physical Oceanography 31, 810–826.

Stommel, H., 1948. The westward intensification of wind-driven ocean currents. Transactions, American Geophysical Union 29, 202–206.

Stommel, H., Arons, A.B., 1960. On the abyssal circulation of the world ocean—I. Stationary planetary flow pattern on a sphere. Deep-Sea Research 6, 140–154.

Stommel, H.M., 1961. Thermohaline convection with two stable regimes of flow. Tellus 13, 224–230.

Straub, D.N., 1996. An inconsistency in between two classical models of the ocean buoyancy driven circulation. Tellus 48A, 477–481.

Sumata, H., Kubokawa, A., 2001. Numerical study of eastern boundary ventilation and its effects on the thermocline structure. Journal of Physical Oceanography 31, 3002–3019.

Toggweiler, J.R., Samuels, B., 1995. Effect of Drake Passage on the global thermohaline circulation. Deep-Sea Research 42, 477–500.

Tsujino, H., Suginohara, N., 1999. Thermohaline circulation enhanced by wind forcing. Journal of Physical Oceanography 29, 1506–1516.

Vallis, G.K., 2006. Atmospheric and Oceanic Fluid Dynamics. Cambridge University Press, 745 pp.

Winton, 1996. The role of horizontal boundaries in parameter sensitivity and decadal-scale variability of coarse-resolution ocean general circulation models. Journal of Physical Oceanography 26, 289–304.

Wright, D.G., Stocker, T.F., 1991. A zonally averaged model for the thermohaline circulation. Part I: Model development and flow dynamics. J. Phys. Oceanogr 21, 1713–1724.

Wright, D.G., Stocker, T.F., Mercer, D., 1998. Closures used in zonally averaged ocean models. J. Phys. Oceanogr 28, 791–804.

Wyrtki, K., 1961. The thermohaline circulation in relation to general circulation in the oceans. Deep-Sea Research 8, 39–64.

Young, W.R., 1981. The vertical structure of the wind-driven circulation. Ph.D. thesis, Joint Program in Oceanography, Massachusetts Institute of Technology – Woods Hole Oceanographic Institution.